Pergamon

Condensation in dust-enriched systems

Denton S. Ebel[1] and Lawrence Grossman*[,1,2]

[1]Department of the Geophysical Sciences, The University of Chicago, 5734 South Ellis Avenue, Chicago, IL 60637, USA
[2]Enrico Fermi Institute, The University of Chicago, 5640 South Ellis Avenue, Chicago, IL 60637, USA

Abstract—Full equilibrium calculations of the sequence of condensation of the elements from cosmic gases made by total vaporization of dust-enriched systems were performed in order to investigate the oxidation state of the resulting condensates. The computations included 23 elements and 374 gas species, and were done over a range of P^{tot} from 10^{-3} to 10^{-6} bar and for enrichments up to 1000× in dust of Cl composition relative to a system of solar composition. Because liquids are stable condensates in dust-enriched systems, the MELTS nonideal solution model for silicate liquids (Ghiorso and Sack, 1995) was incorporated into the computer code. Condensation at 10^{-3} bar and dust enrichments of 100×, 500×, and 1000× occur at oxygen fugacities of IW-3.1, IW-1.7, and IW-1.2, respectively, and, at the temperature of cessation of direct condensation of olivine from the vapor, yields X_{Fa} of 0.019, 0.088, and 0.164, respectively. Silicate liquid is a stable condensate at dust enrichments $>\sim$12.5× at 10^{-3} bar and $>\sim$425× at 10^{-6} bar. At 500×, the liquid field is $>$1000 K wide and accounts for a maximum of 48% of the silicon at 10^{-3} bar, and is 240 K wide and accounts for 25% of the silicon at 10^{-6} bar. At the temperature of disappearance of liquid, X_{Fa} of coexisting olivine is 0.025, 0.14, and 0.31 at 100×, 500×, and 1000×, respectively, almost independent of P^{tot}. At 1000×, the Na_2O and K_2O contents of the last liquid reach 10.1 and 1.3 wt.%, respectively, at 10^{-3} bar but are both negligible at 10^{-6} bar. At 10^{-3} bar, iron sulfide liquids are stable condensates at dust enrichments at least as low as 500× and coexist with silicate liquid at 1000×. No sulfide liquid is found at 10^{-6} bar. At 10^{-3} bar, the predicted distribution of Fe between metal, silicate and sulfide at 1310 K and a dust enrichment of 560× matches that found in H-group chondrites, and at 1330 K and 675× matches that of L-group chondrites prior to metal loss.

Only at combinations of high P^{tot} and high dust enrichment do the bulk chemical composition trends of condensates reach the FeO contents typical of type IIA chondrules at temperatures where dust and gas could be expected to equilibrate, ≥1200 K. Even under these conditions, however, the composition trajectories of predicted condensates pass through compositions with much more $CaO + Al_2O_3$ relative to $MgO + SiO_2$ than those of most type IA chondrules. Furthermore, on a plot of wt.% Na_2O vs. wt.% FeO, most chondrule compositions are too Na_2O-rich to lie along trends predicted for the bulk chemical compositions of the condensates at $P^{tot} \leq 10^{-3}$ bar and dust enrichments ≤1000×. Together, these chemical differences indicate that individual chondrules formed neither by quenching samples of the liquid + solid condensates that existed at various temperatures nor by quenching secondary liquids that formed from such samples. With the exception of very FeO-poor, Na_2O-rich glasses in type I chondrules and glasses with very high FeO and Na_2O in type II chondrules, however, many chondrule glass compositions fall along bulk composition trajectories for liquids in equilibrium with cosmic gases at 10^{-3} bar and dust enrichments between 600× and 1000×. If these chondrules formed by secondary melting of mixtures of condensates that formed at different temperatures, nebular regions with characteristics such as these would have been necessary to prevent loss of Na_2O by evaporation and FeO by reduction from the liquid precursors of their glasses, assuming that the liquids were hot for a long enough time to have equilibrated with the gas. *Copyright © 2000 Elsevier Science Ltd*

1. INTRODUCTION

Several lines of evidence suggest that most chondrites formed at oxygen fugacities significantly higher than those of a solar gas (e.g., Fegley and Palme, 1985; Rubin et al., 1988; Palme and Fegley, 1990; Weinbruch et al., 1990). The most compelling evidence is the high FeO content of chondritic olivine and pyroxene grains, many of which have molar FeO/(FeO + MgO) ratios greater than 0.15 (Wood, 1967; Van Schmus, 1969). Grossman (1972) showed that the first olivine and pyroxene to condense from a cooling solar gas contain only trace amounts of FeO, because iron is more stable as co-condensing metallic nickel–iron. At equilibrium, olivine will not incorporate significant FeO until below 550 K, when iron

metal reacts with gaseous H_2O to form FeO (Grossman, 1972) which must then diffuse into the crystal structure of previously condensed forsterite, replacing MgO. At these low temperatures, however, this mechanism for producing the observed FeO content of olivine in chondrites encounters two fundamental problems: solid–gas equilibrium is unlikely, and diffusion in olivine is very slow. Enhancing the oxygen fugacity of the system in which chondritic matter formed is one way FeO could have been stabilized at temperatures high enough that it was incorporated into ferromagnesian silicates when, or soon after, they first condensed.

The most reasonable mechanism proposed for producing the oxygen fugacity required to form fayalitic olivine at higher temperatures is enhancement of the dust/gas ratio (Wood, 1967; Rubin et al., 1988). In such a model, the initial nebula is a cold cloud of interstellar gas and dust, whose overall composition is

---

solar and in which ~30% of the oxygen is in the dust, and virtually all of the H and C are in the gas. If, before nebular temperatures reach their maximum, dust concentrates in certain regions relative to the gas compared to solar composition, then total vaporization of such regions will produce a gas enriched in oxygen relative to hydrogen and carbon compared to solar composition. Subsequent condensation in such a region occurs in a gas with a significantly higher oxygen fugacity than one of solar composition. Furthermore, the abundance ratios of condensable elements such as Mg and Si to H are increased much more than the O/H ratio, because the dust contains nearly 100% of each of the condensable elements, compared to only 30% of the oxygen. The condensation temperature of any phase increases with increasing partial pressures of its gaseous constituents, which in turn increase with their abundances relative to hydrogen. Dust enrichment therefore not only increases oxygen fugacity, but also increases condensation temperatures, possibly to temperatures at which partial melts are stable.

Wood and Hashimoto (1993) and Yoneda and Grossman (1995) performed full equilibrium calculations of condensation in dust-enriched systems, and both studies found stability fields of silicate liquids at relatively low total pressure. Therefore, an accurate thermodynamic description of silicate liquids is a prerequisite for an accurate description of condensation in dust-enriched systems. Yoneda and Grossman (1995) were the first to assess the stability of nonideal CaO–MgO–Al$_2$O$_3$–SiO$_2$ (CMAS) silicate liquid (Berman, 1983), but were unable to address the stability of ferromagnesian liquids due to lack of an accurate thermodynamic model for silicate liquids containing Fe, Ti, Na, and K.

The present work is the first to explore condensation in either solar composition or dust-enriched systems using a thermodynamic model for ferromagnesian liquids which has been tested against experimental data and natural assemblages. An 11-component subset of the 15-component "MELTS" silicate liquid model, developed by Ghiorso and Sack (1995) to model crystallization of natural silicate liquids of peridotite to intermediate compositions, has been incorporated into condensation calculations. In addition, this liquid model is shown here to describe accurately the crystallization of liquids in the FeO–CMAS system, similar to many of the liquids predicted in this work. Condensation sequences are computed at dust enrichments of up to 1000×, and at P^{tot} of 10^{-3} and 10^{-6} bar, at temperatures from 1100 to 2400 K. Results indicate the composition changes in solid, liquid, and gas phases likely to occur during direct condensation, partial evaporation, or preaccretion metasomatism of matter in dust-enriched systems at these temperatures and pressures. The idea that ferromagnesian chondrules formed by direct condensation in the solar nebula has persisted since Sorby (1877) likened chondrules to solidified "drops of fiery rain", and Wood (1967) revived it by suggesting that liquids of forsterite composition might be stable at low total pressures in gases enriched (by >5000×) in precondensed dust. Therefore, in this work, specific equilibrium assemblages are compared with specific chondrules, and the implications of dust enrichment for chondrule stability in the protoplanetary nebula are explored. Preliminary versions of this work were presented by Ebel and Grossman (1996, 1997a, 1997b, 1998).

2. TECHNIQUE

2.1. Bulk Composition

The nature of the condensates from dust-enriched bulk compositions is strongly influenced by the composition assumed for the dust, and an infinite variety of fractionated dust compositions can be imagined. One constraint on dust composition, however, is that it led to condensate assemblages containing chondritic proportions of condensable elements. Cl chondrites are representative of the bulk composition of the condensable fraction of solar system matter. If the bulk of the condensable elements was originally brought to the solar nebula in the form of interstellar dust, then it is reasonable to assume that the aggregate composition of that dust had a bulk chemical composition similar to that of Cl chondrites. Table 1 shows the relative atomic abundances of the 23 elements considered in this work in solar gas (Anders and Grevesse, 1989), the Cl chondrite dust component of solar gas, and several dust-enriched systems. For a dust enrichment of n, one way to calculate the bulk composition is by adding ($n - 1$) units of the Cl dust to solar composition. Enrichment factors of up to 1000 were investigated. Although there are as yet no astronomical observations that confirm, or astrophysical models that produce such enrichments, there exists no evidence to *rule out* such enrichments in protoplanetary environments.

2.2. Method of Calculation

The condensation code described here, "VAPORS", is described more completely by Ebel et al. (1999). All calculations are normalized to a total of one mole of atoms in the system. A typical condensation run at fixed P^{tot} and bulk composition is begun with only the vapor phase present at 2400 K. Most solutions are obtained at 10 K intervals, using the result at the previous temperature as a first approximation. At each fixed pressure, temperature, and bulk composition of the system, the partial pressures of the pure monatomic gaseous elements (the basis components of the gas phase) are obtained by calculating the distribution of the elements among 374 species in the gas phase, using standard techniques (Lattimer et al., 1978; Smith and Missen, 1982). The stability of each potential, stoichiometrically pure, single component condensate phase is then evaluated from the partial pressures of the elements and the Gibbs energy for that phase, by considering the energy balance of the formation reaction of the condensate from the monatomic gaseous elements. In the case of a liquid or solid solution phase, the "best" composition is determined by finding that composition at which the activities of the components describing the solution phase most closely match equivalent activities in the gas, using the algorithms of Ghiorso (1994). This composition is then tested for stability in much the same way as a stoichiometrically pure condensate, but also accounting for the thermodynamic mixing properties of the components in the solution phase. In some cases where silicate liquid is present, this algorithm failed to find the "best" pyroxene solid solution composition, and the program proceeded with a pure diopside end-member composition instead. In such cases, the program was restarted with a "seed", Ti-, Al-bearing diopsidic pyroxene substituted for the pure diopside at and above the temperature step at which pure diopside had been found to be stable. In all such cases, a complex, Ti-, Al-bearing diopsidic pyroxene was found to be stable at the temperature where pure diopside had been found, or, at most, 20 K higher. The Gibbs energy of the system was always on the order of 0.5 J lower per mole of elements in the system for the assemblage with the pyroxene solid solution than for the one with pure diopside. This problem occurs only with the pyroxene solid solution model, probably because of the difficulty in determining both the composition and ordering state of the near end-member pyroxene in equilibrium with a gas phase highly depleted in some of the pyroxene-forming elements. Once a phase is determined to be stable, it is added to the stable assemblage in a seed amount (10^{-7} mol), which is subtracted from the gas. The next step is to distribute mass between the phases to minimize the total free energy of this new system.

In this work, the second order technique of Ghiorso (1985), following Betts (1980), was adapted to the problem of distributing mass between phases to minimize directly the total Gibbs free energy of a system consisting of gas and multiple pure and solution phases, both

Table 1. Relative atomic abundances in solar composition and the Cl component of solar composition, both normalized to 10^6 atoms Si, and compositions of systems enriched in dust of Cl composition relative to solar.

	Solar	Cl dust	$100 \times$ Cl	$500 \times$ Cl	$1000 \times$ Cl
H	2.79×10^{10}	5.28×10^6	2.84×10^{10}	3.05×10^{10}	3.32×10^{10}
He	2.72×10^9		2.72×10^9	2.72×10^9	2.72×10^9
C	1.01×10^7	7.56×10^5	8.50×10^7	3.87×10^8	7.65×10^8
N	3.13×10^6	5.98×10^4	9.05×10^6	3.30×10^7	6.28×10^7
O	2.38×10^7	7.63×10^6	7.80×10^8	3.83×10^9	7.65×10^9
F	8.43×10^2	8.43×10^2	8.43×10^4	4.22×10^5	8.43×10^5
Ne	3.44×10^6		3.44×10^6	3.44×10^6	3.44×10^6
Na	5.74×10^4	5.74×10^4	5.74×10^6	2.87×10^7	5.74×10^7
Mg	1.07×10^6	1.07×10^6	1.07×10^8	5.37×10^8	1.07×10^9
Al	8.49×10^4	8.49×10^4	8.49×10^6	4.25×10^7	8.49×10^7
Si	1.00×10^6	1.00×10^6	1.00×10^8	5.00×10^8	1.00×10^9
P	1.04×10^4	1.04×10^4	1.04×10^6	5.20×10^6	1.04×10^7
S	5.15×10^5	5.15×10^5	5.15×10^7	2.58×10^8	5.15×10^8
Cl	5.24×10^3	5.24×10^3	5.24×10^5	2.62×10^6	5.24×10^6
Ar	1.01×10^5		1.01×10^5	1.01×10^5	1.01×10^5
K	3.77×10^3	3.77×10^3	3.77×10^5	1.89×10^6	3.77×10^6
Ca	6.11×10^4	6.11×10^4	6.11×10^6	3.06×10^7	6.11×10^7
Ti	2.40×10^3	2.40×10^3	2.40×10^5	1.20×10^6	2.40×10^6
Cr	1.35×10^4	1.35×10^4	1.35×10^6	6.75×10^6	1.35×10^7
Mn	9.55×10^3	9.55×10^3	9.55×10^5	4.78×10^6	9.55×10^6
Fe	9.00×10^5	9.00×10^5	9.00×10^7	4.50×10^8	9.00×10^8
Co	2.25×10^3	2.25×10^3	2.25×10^5	1.13×10^6	2.25×10^6
Ni	4.93×10^4	4.93×10^4	4.93×10^6	2.47×10^7	4.93×10^7

solid and liquid. The Gibbs energy of the entire system can be imagined as a surface in m dimensions, where m is the total number of components independently variable in each of the phases present. The components of the gas are the monatomic elements, while those of solution phases are the end-members of these phases. Each distribution of elements between these components at fixed temperature and pressure defines a state of the system, and corresponds to a point on the Gibbs surface. In successive iterations, information about the local slope and curvature of the Gibbs surface at the current state of the system is used to determine the direction toward a minimum on this surface, along which the next iterative solution must lie. Then atoms are redistributed accordingly among the gas and condensates, that is among the m components, so that this minimum is approached as closely as possible. From the perspective of this new state of the system, the Gibbs surface "looks" different, so a new minimum must be sought in a further iteration. Convergence is declared when the vector norm of all the changes in composition in the m directions does not change by $>10^{-12}$ between iterations. The VAPORS program usually converges in less than 10 iterations in this part of the algorithm.

Upon convergence to a free energy minimum, the stabilities of noncondensed phases are assessed as described above, and if additional phases are found to be stable relative to the gas, they are added as described above and the minimization algorithm is repeated. Even trace phases such as perovskite are typically present at levels $>10^{-6}$ mol per mole of elements in the complete system. If the amount of a phase drops below a minimum value, set at 10^{-10} mol, that phase is removed from the condensate assemblage, and the minimization algorithm is repeated. If no phase must be added or removed after the minimization, the system is considered solved for that temperature, pressure, and bulk composition, and a new temperature step is initiated.

Convergence of each solution is assessed independently by calculation of the difference in the chemical potential of each condensed component between the gas and condensates. For temperatures >1400 K, these differences for each component are always $<10^{-7}$ of the chemical potential in the gas, and usually very much better (e.g., $\sim 10^{-12}$). At lower temperatures, particularly in dust-enriched systems, these differences in some cases increase for components containing the elements Ca, Al, and Ti, and no results are reported here for any temperature step in which the difference exceeds 10^{-4} for any condensate component. Even in an example where these differences are $\sim 3 \times 10^{-4}$, they would record uncertainties corresponding to a shift of only $\sim 10^{-10}$ of the total Ca in the system between the gas and the conden-

sate assemblage. These reaction imbalances occur because the algorithms call for numerical approximation of the first and second derivatives of the Gibbs energy of the gas with respect to the concentration of each of the condensing elements in it, and this approximation becomes increasingly sensitive to machine numerical precision at very low concentrations of elements in the gas (e.g., 10^{-20} mol per mole of elements in the system). Mass balance is preserved to within $<10^{-27}$ of the moles of atoms present throughout all calculations.

2.3. Thermodynamic Data for Elements and Gas Species

In each calculation, 23 elements were included: H, He, C, N, O, F, Ne, Na, Mg, Al, Si, P, S, Cl, Ar, K, Ca, Ti, Cr, Mn, Fe, Co, and Ni. The gas species considered in every calculation include all species considered by Grossman (1972) and Yoneda and Grossman (1995), as well as those listed in Table 2. The $\Delta_f H^\circ$ (298.15 K), S° (298.15 K), and C_p° (T) data for gas species and elements in their standard states were taken wherever possible from the JANAF tables (Chase et al., 1985), obtained in machine readable form from the National Institute of Standards and Technology in 1995. For a few gas species not present in the JANAF database, data from Knacke et al. (1991) or Pedley and Marshall (1983) were used. During calculation, apparent Gibbs energies of formation (Anderson and Crerar, 1993), and hence the equilibrium constants of reactions, were calculated by integration of polynomial fits to tabulated C_p° (T) data. Errors were found in the JANAF tabulations (Chase et al., 1985) of the Gibbs energy of formation ($\Delta_f G^\circ$) and equilibrium constant (ln K_f) for the gas species C_2N_2, C_2H_2, CN, and HS. The error in HS was also present in the electronic version, and had not been previously reported (M. Chase, personal communication; 1996). Although it does not occur in the tabulations of Stull and Prophet (1970), Barin (1989), or Knacke et al. (1991), the $HS_{(g)}$ error has been propagated through the work of Yoneda and Grossman (1995), and probably also Sharp and Wasserburg (1995) and others. The effect of this error is to overestimate the stability of $HS_{(g)}$, and cause $SiS_{(g)}$ to sequester slightly less Si than it should.

2.4. Thermodynamic Data and Models for Solids

The internally consistent thermodynamic database of Berman (1988), or a combination of the internally consistent databases of

Table 2. Gas species and thermodynamic data sources, included in the calculation, in addition to species used by Grossman (1972) and/or Yoneda and Grossman (1995).

Chase et al. (1985)					Other sources
Ne	$CHClF_2$	NiCl	CoF_2	F_3NO	Knacke et al. (1991)
Ar	$CHCl_2F$	ClO	CrN	PF_3O	$CrCl_2O_2$
AlClF	$CHCl_3$	TiOCl	CrO	PF_3	$MnCl_2$
$AlClF_2$	CHF	ClO_2	CrO_2	F_3PS	CrS
$AlCl_2$	CHFO	PCl	CrO_3	SF_3	MnF_2
$AlCl_2F$	CHF_3	ClS	$F_{10}S_2$	SiF_3	NiF_2
$AlCl_3$	CH_2ClF	ClS_2	FeF	TiF_3	$Ni(OH)_2$
AlF_2	CH_2Cl_2	SiCl	FHO	H_4F_4	NiO
AlF_2O	CH_2F_2	TiCl	$SiFH_3$	Mg_2F_4	$NiAl_2Cl_8$
AlF_3	CH_3Cl	Cl_2	SiF_3H	N_2F_4	NiF
$NaAlF_4$	CH_3F	$CoCl_2$	FNO	SF_4	NiH
AlHO	KCN	Cl_2FOP	FNO_2	SiF_4	TiS
Al_2	CN_2*	$FeCl_2$	FNO_3	TiF_4	$CrCl_2$
Al_2Cl_6	CP	$SiCl_2H_2$	FO	TiFO	
Al_2F_6	C_2Cl_2	K_2Cl_2	Na_2Cl_2	PF_5	Pedley and Marshall (1983)
CCl	C_2Cl_4	$SiCl_3$	FO_2	H_5F_5	CoO
CClFO	C_2Cl_6	$NiCl_2$	FPS	H_6F_6	MnO
$CClF_3$	C_2F_2	Cl_2O	SF	SF_6	
CClN	C_2F_4	$TiCl_2O$	SiF	FeS	
CClO	C_2F_6	Cl_2O_2S	F_2	NiS	
CCl_2	C_2HCl	Cl_2S	FeF_2	$K_2O_2H_2$	
CCl_2F_2	C_2HF	Cl_2S_2	H_2F_2	KO	
CCl_2O	C_2H_4	$SiCl_2$	K_2F_2	K_2	
CCl_3	$(KCN)_2$	$TiCl_2$	F_2N	K_2SO_4	
CCl_3F	$Ni(CO)_4$	$CoCl_3$	F_2N_2*	Na_2SO_4	
CCl_4	$Fe(CO)_5$	$SiCl_3F$	Na_2F_2	HNO_2*	
CF	CaCl	$FeCl_3$	F_2O	P_4O_{10}	
CFN	CaS	$SiCl_3H$	SiF_2O	P_4O_6	
CFO	CoCl	$POCl_3$	TiF_2O	P_4	
CF_2	ClF	PCl_3	SF_2O_2	P_4S_3	
CF_2O	$ClFO_2S$	PCl_3S	PF_2	S_3	
CF_3	$ClFO_3$	$TiCl_3$	SF_2	S_4	
CF_4	ClF_2OP	Co_2Cl_4	S_2F_2*	S_5	
CF_4O	ClF_3	Fe_2Cl_4	SiF_2	S_6	
CF_8S	ClF_5	Mg_2Cl_4	FeF_3	S_7	
CHCl	ClF_5S	$SiCl_4$	SiF_2H_2		
$ClNO_2$	FeCl	$TiCl_4$	H_3F_3		
ClHO	PCl_5	$SiCl_3$	H_7F_7		
ClNO	Fe_2Cl_6	NF_3			

* Both *cis* and *trans* forms are included.

Berman and Brown (1985) and Berman (1983) were used wherever possible for all potential condensates in Table 3 and for most end-member components of the solid solution series in Table 4, except for the metal alloy. This means that Berman (1988) was the source of end-member data for the melilite and feldspar solid solutions, not the references cited for the solution models for these phases. The JANAF data (Chase et al., 1985) for pyrrhotite, $Fe_{0.877}S$, are based on estimation of heat capacities from 600 to 1475 K. Recent work below 1000 K by Grønvold and Stølen (1992) indicates that these data cause overstabilization of pyrrhotite by ~5 kJ at 1000 K. Therefore, Gibbs energies of formation of pyrrhotite from the JANAF tables were revised upward by this amount in the calculation. This revision lowers the appearance temperature of pyrrhotite by ~50 K, compared to the JANAF data.

The solid solution models implemented in the MELTS program (circa 1993; Table 4) were used in all calculations, except that Ca-pyroxenes (Sack and Ghiorso, 1994a; 1994b; 1994c) were constrained to have one total atom of Ca + Na per six oxygen atoms. These represent the most comprehensive treatments of the anhydrous igneous rock-forming minerals presently available, and are the solid solution models against which the MELTS silicate liquid model is calibrated. In addition, solid Fe–Ni–Si–Cr–Co alloy was modeled using JANAF data (Chase et al., 1985) for pure metal end-members, and an asymmetric binary solution model calibrated against activity data for the binary systems of Chuang et al. (1986b) for Fe–Ni, Sakao and Elliott (1975) for Fe–Si, and Normanton et al. (1976) for Fe–Cr, with Fe–Co treated

as ideal. Such a calibration is justifiable for the dilute alloys found at high temperature in this work.

Some cations of great interest in condensation are not contained in some of the liquid or solid solution models used here. These are the first condensation calculations in which the TiO_2 content of spinel is modeled, and extraordinarily high TiO_2 contents are predicted at very high temperatures. In all such cases, however, spinel coexists with a CMAS liquid into which TiO_2 is artificially prevented from dissolving. Partitioning experiments (Connolly and Burnett, 1999) suggest that these high TiO_2 contents may be spurious. Insufficient experimental work exists to justify inclusion of Ti^{3+} or Cr^{3+} in the pyroxene model. No solution model is used for Mn, S, P, or C in the metal alloy, and this could artificially enhance the stabilities of troilite, pyrrhotite, and whitlockite. Similarly, our inability to account for Ni or Co in troilite or pyrrhotite, nor for Cr, Ti, or Al in olivine, may artificially destabilize these phases slightly. Although Hirschmann (1991) has modeled Ni, Co, and Mn in olivine, these elements are not addressed by the pyroxene model, nor are Ni and Co included in the spinel model employed here. Because inclusion of Ni, Co, or Mn in only one of these phases would artificially stabilize that phase and cause it to contain excessive amounts of these cations, these cations were not included in the olivine model. This omission, however, artificially stabilizes $MnTiO_3$-rich rhombohedral oxide solid solutions and crystalline MnO.

Table 3. Pure solid phases considered in the calculation, and sources of thermodynamic data.

Miscellaneous solid phases[a]			Chase et al. (1985)	
Aenigmatite	$Na_2Fe_5TiSi_6O_{20}$	M		
Andalusite	Al_2SiO_5	B8	Al	MgS
Anhydrite	$CaSO_4$	R	Al_4C_3	Mg_2Si
Anthophyllite	$Mg_7Si_8O_{22}(OH)_2$	B8	AlN	$MgSO_4$
Apatite	$Ca_5(PO_4)_3OH$	M	Al_2S_3	$MgTi_2O_5$
Brucite	$Mg(OH)_2$	B8	$Al_6Si_2O_{13}$	Na
Ca-aluminate	$CaAl_2O_4$	B5	alpha Ca	alpha Na_3AlF_6
Calcite	$CaCO_3$	B8	beta Ca	beta Na_3AlF_6
Cohenite	Fe_3C	R	$CaCl_2$	$NaAlO_2$
Cordierite	$Mg_2Al_4Si_5O_{18}$	B8	CaF_2	NaCl
Corundum	Al_2O_3	B8	$Ca(OH)_2$	NaCN
Cristobalite	SiO_2	M	CaS	Na_2CO_3
Dolomite	$CaMg(CO_3)_2$	B8	CoO	NaF
Grossite	$CaAl_4O_7$	B5	Cr_3C_2	NaH
Hatrurite	Ca_3SiO_5	B5	CrN	NaO_2
Hibonite	$CaAl_{12}O_{19}$	B3	Cr_2N	Na_2O
Kalsilite	$KAlSiO_4$	M	Cr_2O_3	Na_2O_2
Leucite	$KAlSi_2O_6$	M	$FeCl_2$	NaOH
Lime	CaO	B8	FeF_2	Na_2S
Magnesite	$MgCO_3$	B8	$Fe_{0.947}O$	Na_2S_2
Manganosite	MnO	R	FeO	Na_2SiO_3
Merwinite	$Ca_3MgSi_2O_8$	B8	$Fe(OH)_2$	$Na_2Si_2O_5$
Nepheline	$NaAlSiO_4$	M	$Fe(OH)_3$	Na_2SO_4(I-V)
Periclase	MgO	B8	FeS_2 (Pyrite)	NH_4Cl
Perovskite	$CaTiO_3$	R	$FeSO_4$	P
Pyrrhotite	$Fe_{0.877}S$	J	$Fe_2(SO_4)_3$	monocl S
Quartz	SiO_2	M	Graphite	ortho S
Rankinite	$Ca_3Si_2O_7$	B5	K	alpha SiC
Rutile	TiO_2	B8	KCl	beta SiC
Sapphirine	$Mg_4Al_{10}Si_2O_{23}$	B3	KF	Si_3N_4
Sillimanite	Al_2SiO_5	B8	KF_2H	SiS_2
Sinoite	Si_2N_2O	F	KH	alpha Ti
Sphene	$CaTiSiO_5$	B8	K_2O	beta Ti
Talc	$Mg_3Si_4O_{10}(OH)_2$	B8	KOH	TiC
Tialite	Al_2TiO_5	R	K_2S	TiH_2
Tri-Ca aluminate	$Ca_3Al_2O_6$	B5	K_2SO_4	TiN
Tridymite	SiO_2	M	K_2SiO_3	alpha TiO
Troilite	FeS	C	Mg	beta TiO
Whitlockite	$Ca_3(PO_4)_2$	M	MgC_2	Ti_2O_3
Wollastonite	$CaSiO_3$	B8	Mg_2C_3	Ti_4O_7
			$MgCl_2$	alpha Ti_3O_5
			MgH_2	beta Ti_3O_5
			MgF_2	
			Mg_3N_2	

[a] Symbols for data are: B5 = Cp from Berman and Brown (1985), 298 K data from Berman (1983); B3 = Berman (1983); B8 = Berman (1988); C = Hsieh et al. (1987); R = Robie et al. (1978); F = Fegley (1981); M = 'MELTS' software database (Ghiorso and Sack, 1995); J = Chase et al. (1985) modified for consistency with Grønvold and Stølen (1992).

2.5. Thermodynamic Data and Models for Silicate Liquids

A major innovation in the work presented here is the inclusion of the "MELTS" model for silicate liquids (Ghiorso, 1985; Ghiorso and Sack, 1995), which describes the thermodynamic properties of silicate liquids using a regular (symmetric) binary solution model in the components SiO_2–TiO_2–Al_2O_3–Fe_2O_3–Fe_2SiO_4–Mg_2SiO_4–$MgCr_2O_4$–$CaSiO_3$–Na_2SiO_3–$KAlSiO_4$–$Ca_3(PO_4)_2$–H_2O, in addition to $MnSi_{0.5}O_2$–$NiSi_{0.5}O_2$–$CoSi_{0.5}O_2$ which have been omitted in the present study. Crystallization calculations with MELTS have been found to yield remarkable agreement between calculated and observed amounts and compositions of phases in liquid-crystal equilibrium experiments at 1 bar (Ghiorso and Carmichael, 1985) and at 10 kbar (Baker et al., 1995; Hirschmann et al., 1998). Ghiorso and Sack (1995) caution against using their model: (a) in systems containing only a small subset (<7) of the components, or (b) far outside the temperature–pressure–composition range of its calibration. Both of these *caveats* are addressed below.

2.5.1. Test of MELTS: Peridotite KLB-1

Anticipating that condensate liquids will be poor in non-CMAS components and will thus violate *caveat* (a), we tested MELTS calculations against quenched partial melting experiments of peridotite KLB-1, whose non-CMAS components consist of only 8.1 wt.% FeO, and ≤0.3% of all other oxides. Takahashi (1986) and Takahashi et al. (1993) reported the temperature intervals between the observed absence and presence of phases, as well as phase compositions and melt fractions for KLB-1 at 1 bar at the Ni–NiO oxygen buffer. Note that only one of their seven data points used here is used in the MELTS calibration database. It can be seen in Figure 1 that the MELTS model reproduces the observed volume fractions of liquids well, except at low melt fractions where there may be significant measurement error in the experiments. The solidus temperature and appearance temperatures of olivine, Ca–pyroxene, and feldspar agree nearly within experimental error, but the model underpredicts the crystallization temperature of orthopyroxene and overpredicts that of spinel (Table 5). Hirschmann et

Table 4. Solid solutions considered in the calculation, and sources of solution models.

Metal alloy (this work)	
Iron	Fe
Nickel	Ni
Silicon	Si
Chromium	Cr
Cobalt	Co
Olivine (Sack and Ghiorso, 1989; 1994b)	
Fayalite	Fe_2SiO_4
Forsterite	Mg_2SiO_4
Monticellite	$CaMgSiO_4$
Melilite (Charlu et al., 1981)	
Åkermanite	$Ca_2MgSi_2O_7$
Gehlenite	$Ca_2Al_2SiO_7$
Orthopyroxene (Sack and Ghiorso, 1989; 1994b)	
Enstatite	$Mg_2Si_2O_6$
Ferrosilite	$Fe_2Si_2O_6$
Ca-pyroxene (Sack and Ghiorso, 1994a; 1994b; 1994c)	
Diopside	$CaMgSi_2O_6$
Hedenbergite	$CaFeSi_2O_6$
Alumino-buffonite	$CaTi_{0.5}Mg_{0.5}AlSiO_6$
Buffonite	$CaTi_{0.5}Mg_{0.5}FeSiO_6$
Essenite	$CaFeAlSiO_6$
Jadeite	$NaAlSi_2O_6$
Feldspar (Elkins and Grove, 1990)	
Albite	$NaAlSi_3O_8$
Anorthite	$CaAl_2Si_2O_8$
Sanidine	$KAlSi_3O_8$
Spinel (Sack and Ghiorso, 1991a; 1991b)	
Chromite	$FeCr_2O_4$
Hercynite	$FeAl_2O_4$
Magnetite	Fe_3O_4
Spinel	$MgAl_2O_4$
Ulvospinel	Fe_2TiO_4
Rhombohedral oxide (Ghiorso, 1990)	
Geikielite	$MgTiO_3$
Hematite	Fe_2O_3
Ilmenite	$FeTiO_3$
Pyrophanite	$MnTiO_3$

al. (1998) observed that the MELTS model *over*predicted the crystallization temperature of orthopyroxene at 10 kbar. These differences reflect compromises made by Sack and Ghiorso (1994c) to best satisfy both high- and low-pressure pyroxene–liquid phase relations. In Figure 2, the 1 bar liquid compositions are compared with MELTS results, with all Fe_2O_3 recalculated to FeO. The good agreement of the results for melt fraction and composition suggests that the MELTS model will yield reasonably accurate results in the condensation calculation, particularly because olivine dominates the distribution of mass in condensation sequences. Because spinel is a minor phase, overstabilization of spinel will not have a significant effect on liquid stability. The understabilization of orthopyroxene, relative to liquid, suggests that liquid stability might be slightly overpredicted when orthopyroxene condenses with it, and that the temperature of appearance of the latter phase in the condensation calculation may be too low.

In addition to MELTS, Berman's (1983) model for CMAS liquids is included in the present work. Yoneda and Grossman (1995) used this model, and explained in detail its advantages and drawbacks. The CMAS liquid model works well at high temperatures, where these four oxides are the only major ones condensed, but it is inadequate under conditions where FeO, Na_2O, and other non-CMAS components condense in appreciable quantities. Therefore, the MELTS model must be

used at lower temperatures where non-CMAS oxides are important constituents of the liquid. The purely CMAS liquid region is very far outside the composition range over which MELTS is calibrated, and contains too few components for reliable application of the MELTS liquid model. Furthermore, because the MELTS liquid uses mostly silicate components, not pure oxides as end-members, it cannot be applied to some especially Ca- and Al-rich regions of composition space that are treated adequately by the CMAS liquid model. For example, $CaSiO_3$ is the major Ca-containing component employed by MELTS; yet, early high temperature condensate liquids never contain as much SiO_2 as CaO. For these reasons, both models are required to completely describe condensation of silicate liquids over the temperature ranges where liquids may be stable.

2.5.2. Transition between liquid models

A decision must be made as to when to switch from one model to the other. In order to model non-CMAS oxides in the liquid, it would be best to switch to the MELTS model at the highest feasible temperature. For the case of 100× dust enrichment at $P^{tot} = 10^{-3}$ bar, the curves in Figure 3 illustrate the major oxide compositions of the two liquids, calculated at 2 K intervals, near the appearance temperature of olivine, indicated by the vertical line at 1782 K. The CMAS liquid is CaO- and Al_2O_3-rich at high temperatures, but SiO_2 and MgO increase rapidly with decreasing temperature. By contrast, although a MELTS liquid becomes stable well above 1782 K, it is CaO-deficient and SiO_2-enriched, relative to the CMAS liquid, because the only liquid the MELTS model can determine to be stable must have sufficient SiO_2 to supply the required $CaSiO_3$ component. That is, in the temperature range above at least 1790 K, the most stable liquid possible in the MELTS composition range is not the liquid which *should* be stable. When the temperature of olivine appearance is reached, however, the MELTS liquid has gained sufficient SiO_2 and MgO to have a composition very similar to the CMAS liquid at the same temperature. Once sufficient SiO_2 has condensed, the MELTS model closely tracks the Berman (1983) model liquid, but also accounts for increasing FeO and TiO_2 contents.

It was determined by performing condensation calculations with each liquid separately that the CMAS liquid and the MELTS liquid have nearly identical compositions at the temperature where olivine becomes stable with CMAS liquid for $10^{-6} \leq P^{tot} \leq 10^{-3}$, and 15× ≤ dust enrichment ≤ 1000×. The criterion of olivine stability is, therefore, used to trigger a switch from the CMAS liquid model to the MELTS silicate liquid model in the calculations. The similarity in oxide concentrations below the olivine stability temperature (Fig. 3) could be expected from the similarity of the Berman (1983) database, against which the CMAS model was calibrated, and the Berman (1988) database, upon which the MELTS model relies. These comparisons strongly suggest that the *caveats* cited by Ghiorso and Sack (1995) regarding use of the MELTS liquid model are not egregiously violated in its use below the condensation temperature of olivine.

3. RESULTS

3.1. Vapor of Solar Composition

Different thermodynamic data are employed for some crystalline phases, many more chemical species are included, and a very different computational procedure was used in the present study than in our previous work on condensation (Yoneda and Grossman, 1995). It is therefore important to compare results from the two studies, and this is done for the case of a solar gas at $P^{tot} = 10^{-3}$ bar in Table 6. Appearance temperatures of phases refer to the highest temperature step at which a phase is part of the condensate assemblage in the 2 K steps of the calculations. Our results are quite similar, but not identical, to those of Yoneda and Grossman (1995), referred to as the previous work in the following explanation of the differences which, in all cases, are due to differences in thermodynamic data. Note that, although some of the data used in our previous
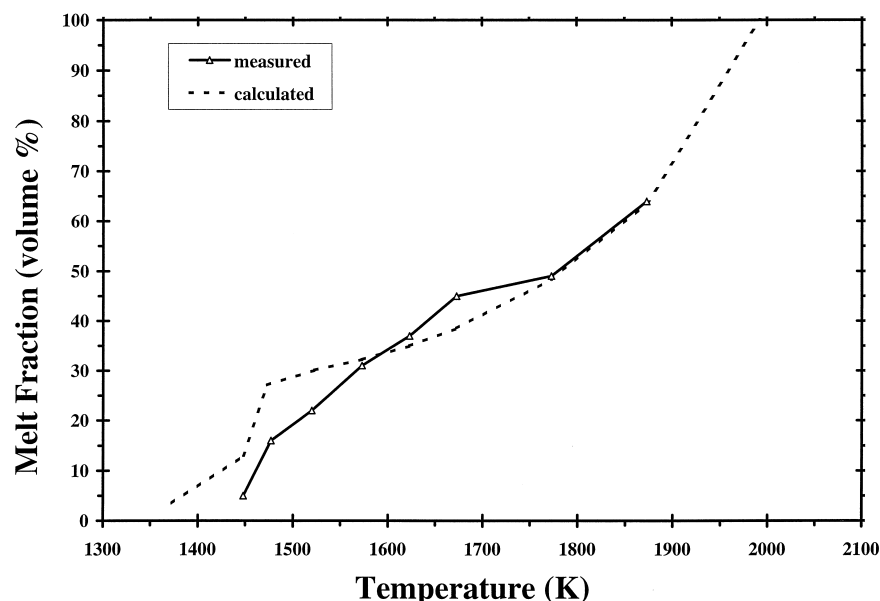
Fig. 1. Comparison of melt fractions measured in peridotite melting experiments of Takahashi (1986) and Takahashi et al. (1993) with those calculated at 1 bar using MELTS.

work may be more accurate, e.g., those for hibonite and grossite, we use those in Table 3 in the present study because the latter are more consistent with the MELTS liquid model. Hibonite forms from corundum 15 K lower in the present calculations than in the previous work because hibonite is 2.5 kJ less stable and corundum is 0.3 kJ more stable at 1700 K in the present work. The lesser stability of hibonite in the present work allows it to be replaced by grossite and $CaAl_2O_4$, which are 16.7 and 8.7 kJ more stable, respectively, at 1700 K in the present work. Here the gehlenite end-member of the melilite solid solution series is 10.1 kJ less stable at 1600 K than it was previously, and it forms from $CaAl_2O_4$, a phase more stable than hibonite in the present calculations. This causes the appearance temperature of melilite to be suppressed by nearly 50 K and allows grossite and hibonite to partially replace it at lower temperature. Spinel condenses 13 K lower in the present work than it did previously, primarily because the $MgAl_2O_4$ end-member is now 3.5 kJ less stable at 1500 K. Plagioclase forms from spinel ~10 K lower in the present work because the $CaAl_2Si_2O_8$ end-member is 6.5 kJ less stable at 1400 K than it was previously. In the present work, Ti_3O_5 forms from Ti-

bearing clinopyroxene 18 K lower and Ti_4O_7 does not form at all because of gross differences in the way the Ti-bearing end-member components are treated in the two calculations. In the previous work, literature data were used for the Ti^{3+}-

Fig. 2. Comparison of measured compositions of KLB-1 liquids (Takahashi, 1986; Takahashi et al., 1993) with those calculated from MELTS, all at 1 bar. Asterisks indicate starting compositions in the experiments.

Table 5. Comparison of experimental phase appearance temperatures (Takahashi, 1986, run 4) with MELTS calculation for KLB-1, all at 1 bar.

	Temperature (K)	
	Reported	Predicted by MELTS
Olivine in:	>1973	1993
Spinel in:	1723–1773	1838
Orthopyroxene in:	1573–1623	1498
Ca-rich pyroxene in:	1473–1523	1473
Feldspar in:	1423–1448	1463
Liquid out:	1373–1423	1368
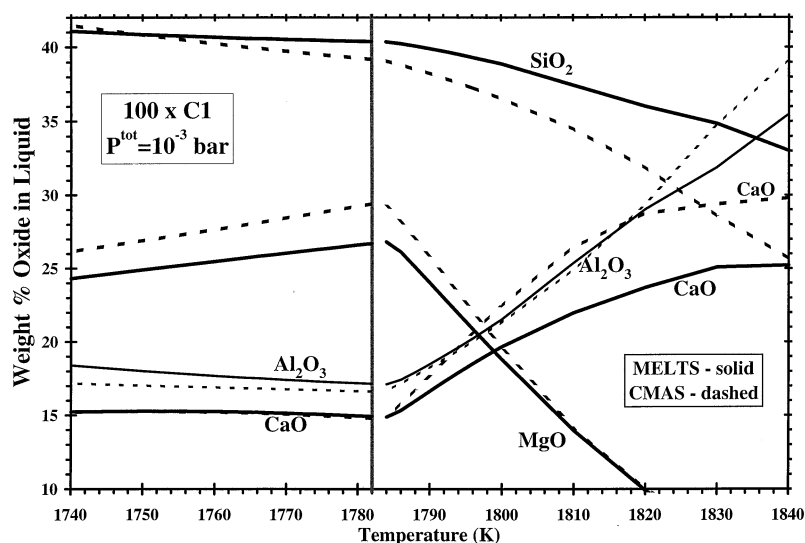
Fig. 3. Compositions of CMAS and MELTS liquids near the olivine appearance temperature (vertical line at 1782 K) at the stated conditions. In this temperature range, the MELTS liquid also contains ~1 wt.% of other oxides, which are not shown.

bearing component $CaTiAlSiO_6$ and estimated for the Ti^{4+}-bearing component $CaTiAl_2O_6$ while, in the present work, only data for the Ti^{4+}-bearing components $CaTi_{0.5}Mg_{0.5}AlSiO_6$ and $CaTi_{0.5}Mg_{0.5}FeSiO_6$ are used. Cordierite replaces plagioclase in the present work because it is 12.8 kJ/mol more stable, and plagioclase is 7.2 kJ less stable, at 1300 K relative to the previous work. Sphene does not form above 1200 K in the present work because it is 5.5 kJ/mol less stable than it was previously. No liquids were found to be stable in solar gas at $P^{tot} = 10^{-3}$ bar by us or any previous workers, e.g., Wagner

(1979), Wood and Hashimoto (1993), and Yoneda and Grossman (1995), despite a contrary claim by Wark (1987).

3.2. General Effects of Dust Enrichment and P^{tot}

Complete condensation calculations were performed from 2400 K down to the last temperature step where our criteria for adequate convergence could be met, usually between 1100 and 1300 K, and up to dust/gas enrichment factors of 1000× relative to solar composition, hereinafter abbreviated as "dust

Table 6. Temperatures (K) of appearance and disappearance of condensates from a gas of solar composition at $P^{tot} = 10^{-3}$ bar, compared with earlier results.

Mineral	This work		Yoneda and Grossman (1995)	
	In	Out	In	Out
Corundum	1770	1726	1770	1740
Hibonite	1728	1686	1743	1500
Grossite	1698	1594		
Perovskite	1680	1458	1688	1448
CaAl$_2$O$_4$	1624	1568		
Melilite ss.	1580	1434	1628	1444
Grossite	1568	1502		
Hibonite	1502	1488		
Spinel ss.	1488	1400	1501	1409
Metal ss.	1462		1464	
Clinopyroxene ss.	1458		1449	
Olivine ss.	1444		1443	
Plagioclase ss.	1406	1318	1416	
Ti$_3$O$_5$	1368	1342	1386	1361
Orthopyroxene ss.	1366		1366	
Ti$_4$O$_7$			1361	1217
Cordierite	1330			
Cr–spinel ss.	1230		1221	
Sphene			1217	
End of computation	1200		970	

Table 7. Temperatures (K) of appearance and disappearance of condensates at $P^{tot} = 10^{-6}$ bar as a function of dust/gas enrichment.

Dust/gas enrichment:	1×		100×		500×		1000×	
Condensate	In	Out	In	Out	In	Out	In	Out
Corundum	1570	1470	1890	1790	2010	1930	2040	1980
Hibonite	1480	1430	1790	1750	1940	1890	1980	1950
Perovskite	1460	1270	1690	1500	1760	1610	1740	1670
Grossite	1440	1370	1760	1650	1910	1780	1960	1820
CaAl$_2$O$_4$	1390	1360	1680	1620	1820	1740		
Melilite	1370	1250	1630	1470	1760	1740		
Grossite	1360	1300	1620	1550	1740	1670		
Liquid					1740	1730	1880	1370
Melilite					1730	1630		
Hibonite	1320	1270	1550	1540				
Spinel	1270	1210	1540	1430	1670	1610	1720	1660
Liquid					1630	1390		
Clinopyroxene	1270		1500		1430		1370	
Olivine	1240		1490		1610		1660	
Sapphirine	1230	1190						
Metallic nickel–iron	1210		1360		1420		1430	
Plagioclase	1210	1190	1440	1300	1450		1410	
Cordierite	1200		1310					
Orthopyroxene	1190		1400		1490		1530	1230
Cr–spinel	1160		1410		1610		1660	
Pyrophanite			1130		1230		1250	
MnO			1090		1180		1210	
End of computation	1100		1090		1160		1200	

enrichments of 1000×". The extremes of 10^{-3} and 10^{-6} bar were chosen to bracket the generally accepted range of P^{tot} in the inner solar nebula (Wood and Morfill, 1988). Results are shown at four different dust enrichments at 10^{-6} bar in Table 7 and at 10^{-3} bar in Table 8. In these tables, appearance and disappearance temperatures are defined as the highest temperature steps at which a phase is either part of or becomes absent from the stable condensate assemblage. In figures showing elemental distributions among coexisting phases, the fraction of an element present in a phase at its appearance temperature is extrapolated to zero in the next highest temperature step.

3.2.1. Oxygen fugacity

Shown in Figure 4 is the temperature dependence of the oxygen fugacity of the gas in equilibrium with condensate

Table 8. Temperatures (K) of appearance and disappearance of condensates at $P^{tot} = 10^{-3}$ bar as a function of dust/gas enrichment.

Dust/gas enrichment:	1×		100×		500×		1000×	
Condensate	In	Out	In	Out	In	Out	In	Out
Liquid			2200	1390	>2400	1400	>2400	1310
Corundum	1770	1720						
Hibonite	1720	1680						
Grossite	1690	1590						
Perovskite	1680	1450	1970	1810				
CaAl$_2$O$_4$	1620	1560						
Melilite	1580	1430						
Grossite	1560	1500						
Hibonite	1500	1480						
Spinel	1480	1400	1830	1710	1990	1940	2050	1990
Metallic nickel–iron	1460		1690		1780		1800	
Clinopyroxene	1450		1440		1420		1390	
Olivine	1440		1780		1940		1990	
Plagioclase	1400	1310	1450		1430		1430	
Orthopyroxene	1360		1620		1700			
β-Ti$_3$O$_5$	1360	1340						
Cordierite	1330							
Cr–spinel	1230		1600		1760		1710	
Pyrophanite			1350		1400		1380	
MnO			1300		1420		1480	
Pyrrhotite					1330		1380	
Whitlockite							1350	
End of computation	1210		1200		1240		1260	
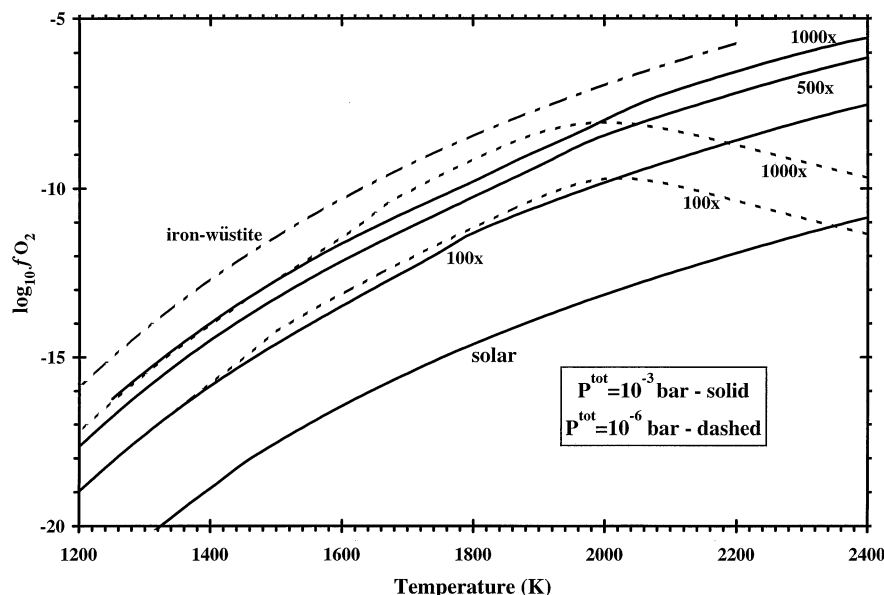
Fig. 4. Variation of oxygen fugacity with temperature for gas in equilibrium with condensates at the stated conditions of total pressure and dust enrichment, with the iron–wüstite buffer curve (dash-dot pattern) shown for reference.

assemblages computed at dust enrichments of $100\times$, $500\times$, and $1000\times$ at $P^{tot} = 10^{-3}$ bar, and at dust enrichments of $100\times$ and $1000\times$ at 10^{-6} bar, along with that of the iron–wüstite buffer ($\log f_{O_2} = IW$) and that of a gas of solar composition at 10^{-3} bar ($\log f_{O_2} \sim IW-6$) for reference. The curves for $P^{tot} = 10^{-3}$ bar are nearly concentric with one another and show the expected increase of f_{O_2} with increasing dust enrichment. The curves for dust enrichments of $100\times$, $500\times$, and $1000\times$ lie at about IW-3.1, IW-1.7, and IW-1.2, respectively. Exceptions to this concentric behavior are seen as subtle changes in curvature, particularly noticeable at high dust enrichments where the onset of olivine condensation removes significant fractions of the oxygen from the vapor. Comparison of the two curves for a constant dust enrichment of $100\times$ shows a slight increase in f_{O_2} by as much as 0.4 log units as P^{tot} drops from 10^{-3} to 10^{-6} bar below 2000 K. The smallness of the variation with P^{tot} is due to the fact that f_{O_2} in oxygen-rich cosmic gases is largely controlled by the equilibrium $H_2 + \frac{1}{2}O_2 = H_2O$, and therefore depends on the P_{H_2O}/P_{H_2} ratio which is almost independent of P^{tot} at a given temperature, as discussed by Yoneda and Grossman (1995). Above 2000 K, however, Fig. 4 shows that, at dust enrichments of $100\times$ and $1000\times$, the f_{O_2} values at 10^{-6} bar drop below their respective values at 10^{-3} bar and the difference in f_{O_2} between the two total pressures at constant dust enrichment increases with increasing temperature, reaching nearly 4 log units at 2400 K. This exceptionally large variation in f_{O_2} with P^{tot} is due to the fact that, at 10^{-6} bar, almost all of the H_2 and H_2O are dissociated into monatomic species at these high temperatures, making the above equilibrium irrelevant to the f_{O_2} while, at 10^{-3} bar, this dissociation occurs above 2400 K because the higher pressure favors polyatomic over monatomic species.

3.2.2. Condensation temperatures and stability of liquid

The progressive increase in condensation temperatures of all phases with increasing dust enrichment at constant P^{tot}, as seen by Yoneda and Grossman (1995), is illustrated in Tables 7 and 8. At 10^{-6} bar, condensation temperatures are still low enough at a dust enrichment of $100\times$ that no liquid phase is stable. However, at this P^{tot} and above a dust enrichment between $400\times$ and $450\times$, the oxide + silicate fraction of the assemblage that condenses in certain temperature intervals, does so at a temperature above the solidus temperature for its bulk chemical composition, causing liquid to be a stable condensate. Upon cooling a system at 10^{-6} bar and a dust enrichment of $500\times$, liquid first appears at 1740 K, where melilite and $CaAl_2O_4$ react with the gas to form grossite and a CMAS liquid. This liquid field persists for only 10 K, at which point it crystallizes into melilite and grossite. A liquid field reappears at 1630 K by reaction of melilite with the gas, and persists to 1390 K. At 10^{-6} bar and a dust enrichment of $1000\times$, condensation of all phases occurs at even higher temperatures such that a much greater range of bulk condensate compositions forms above solidus temperatures, causing the liquid stability field to extend to higher temperature, 1880 K, and to persist without interruption to 1370 K, replacing the stability fields of $CaAl_2O_4$, melilite, and grossite.

At constant dust enrichment, condensation temperatures of all phases are higher at 10^{-3} bar than at 10^{-6} bar because partial pressures of most condensable elements increase with P^{tot}. As a result, the minimum dust enrichment necessary to condense partial melts at 10^{-3} bar is considerably lower than at 10^{-6} bar, and lies between $12\times$ and $13\times$. At 10^{-3} bar, there is, at a dust enrichment of only $100\times$, an extensive and uninterrupted stability field of liquid extending up to 2200 K and replacing the stability fields of corundum, hibonite, grossite, $CaAl_2O_4$, and melilite. At higher dust enrichments at this P^{tot}, the liquid stability field extends to even higher temperatures.

One way of viewing trends in the size of the liquid stability field as a function of P^{tot} and dust enrichment is by comparison of graphs of the distribution of silicon between condensed phases and vapor vs. temperature. Such diagrams are presented
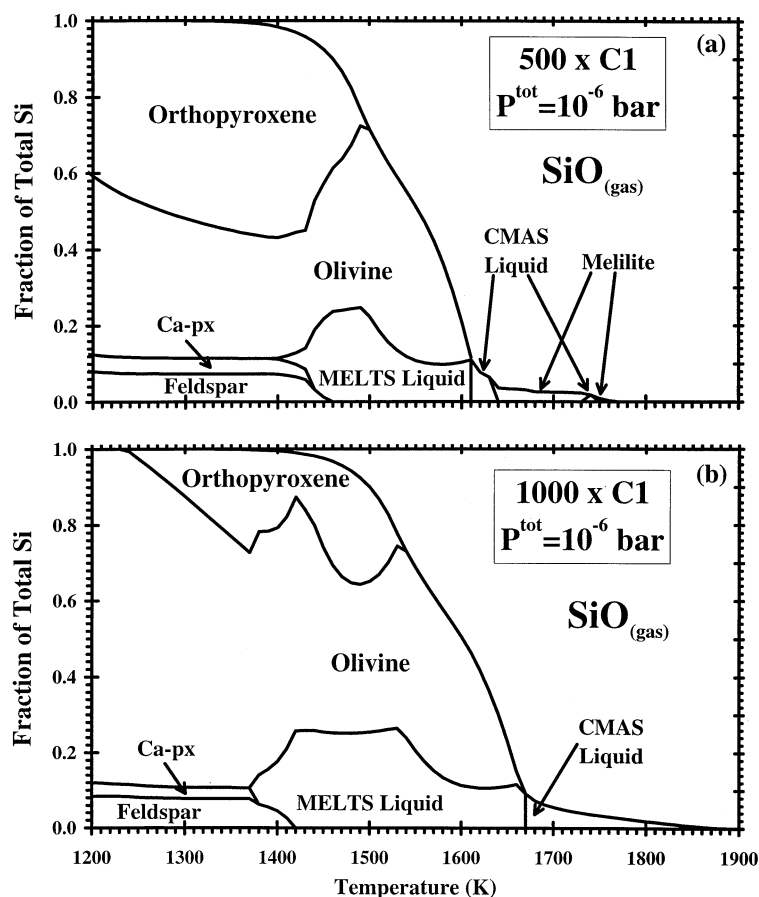
Fig. 5. Distribution of Si between condensed phases and gas at $P^{tot} = 10^{-6}$ bar and a dust enrichment of (a) 500×; and (b) 1000×. Ca-px = Ca-rich clinopyroxene.

in Figs. 5a and 5b for 10^{-6} bar and dust enrichments of 500× and 1000×, respectively, and should be compared to Figures 6d and 7d for the cases of 100× and 1000×, respectively, at 10^{-3} bar. At 10^{-3} bar, the liquid has a stability field 800 K wide (Table 8) and accounts for a maximum of 32% of the silicon at a dust enrichment of 100×. At the same P^{tot}, the liquid field widens to >1100 K, with a maximum of 60% of the silicon, at a dust enrichment of 1000×. Although both the temperature interval for the stability of liquid and the maximum fraction of the total silicon accounted for by the liquid are always smaller at 10^{-6} bar than at 10^{-3} bar for the same dust enrichment, the liquid fields at 10^{-6} bar are still quite extensive at these elevated dust enrichments. For example, although a very small, high-temperature field of liquid is separated from a lower-temperature liquid field at 500×, the latter field is 240 K wide and accounts for a maximum of 25% of the silicon and, at 1000×, the liquid field is over 500 K wide and accounts for a maximum of 26% of the silicon. Petaev and Wood (1998) found no liquid stability field at 10^{-5} bar and a dust enrichment of 10^7. This is in clear disagreement with the results of Wood and Hashimoto (1993) who found a small liquid stability field at the same P^{tot} and a lower dust enrichment, 10^3, as both studies employed the same liquid solution model and dust composition. The Petaev and Wood (1998) results are also in complete disagreement with ours in that we find a liquid

stability field at both lower P^{tot} and lower dust enrichment. Although the existence of a liquid stability field in Wood and Hashimoto's (1993) study is in general agreement with the work presented here, both the amount of liquid and the temperature interval of its stability are much smaller than would be expected from our work, presumably because of Wood and Hashimoto's (1993) use of an ideal solution model for silicate liquids, which are demonstrably nonideal (Berman, 1983; Ghiorso et al., 1983), and the difference between their assumed dust composition and ours.

From Tables 7 and 8, it is clear that the assemblage liquid + metallic nickel–iron + olivine + orthopyroxene + Cr–spinel occupies a very wide stability field within the ranges of P^{tot} and dust enrichment considered herein.

3.3. Condensation at 100× Dust Enrichment and $P^{tot} = 10^{-3}$ Bar

The distributions of Al, Mg, Ca, Si, Fe, and Na and K between condensed phases and vapor are illustrated in Figs. 6a, 6b, 6c, 6d, 6e, and 6f, respectively, for a system enriched 100× in dust at $P^{tot} = 10^{-3}$ bar. The first condensate, a CMAS liquid extremely rich in Al_2O_3 (79 mol%) and CaO (21%) with only minor amounts of MgO and SiO_2, condenses at 2200 K. Perovskite becomes stable at 1970 K, and consumes 85% of the
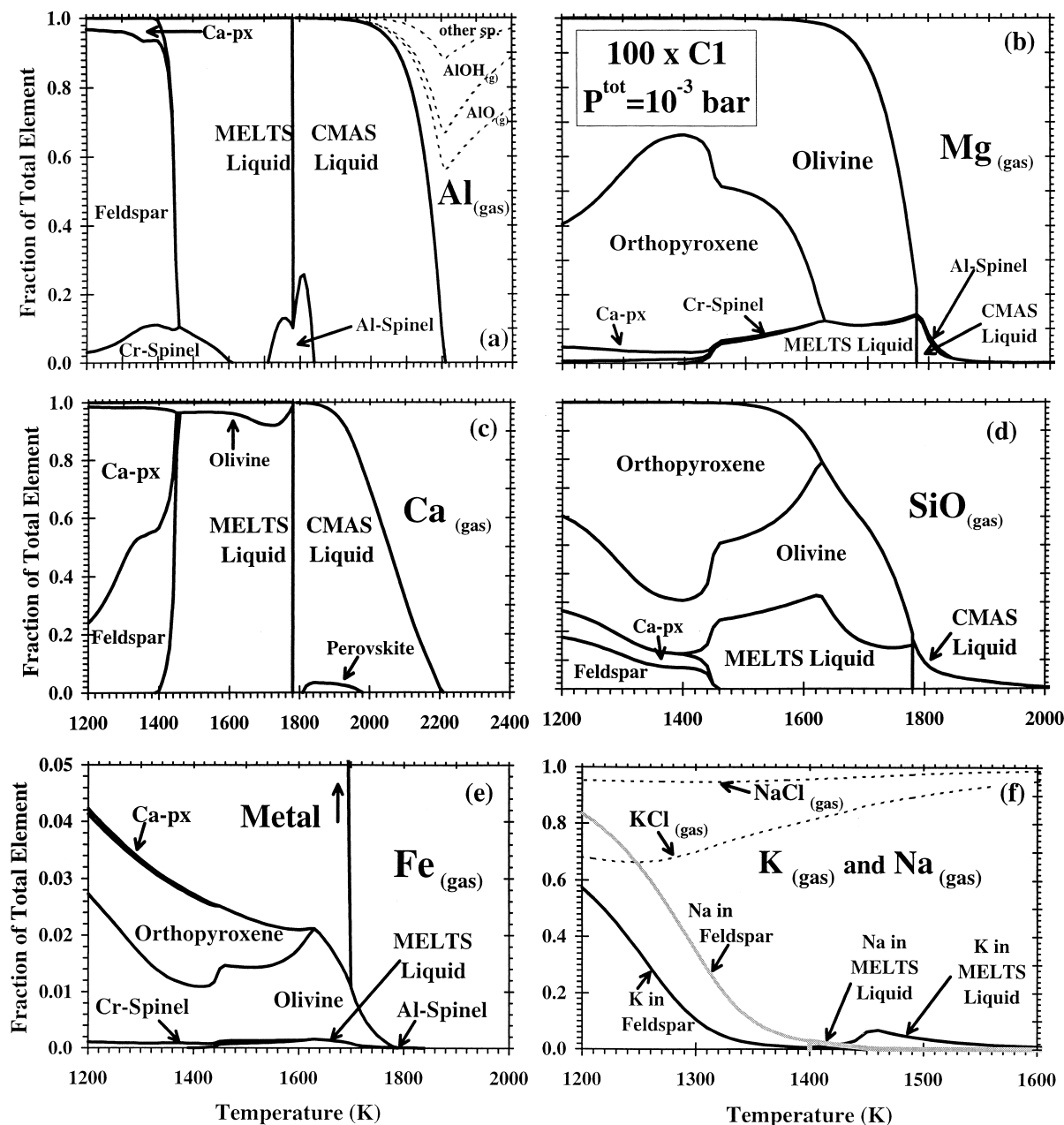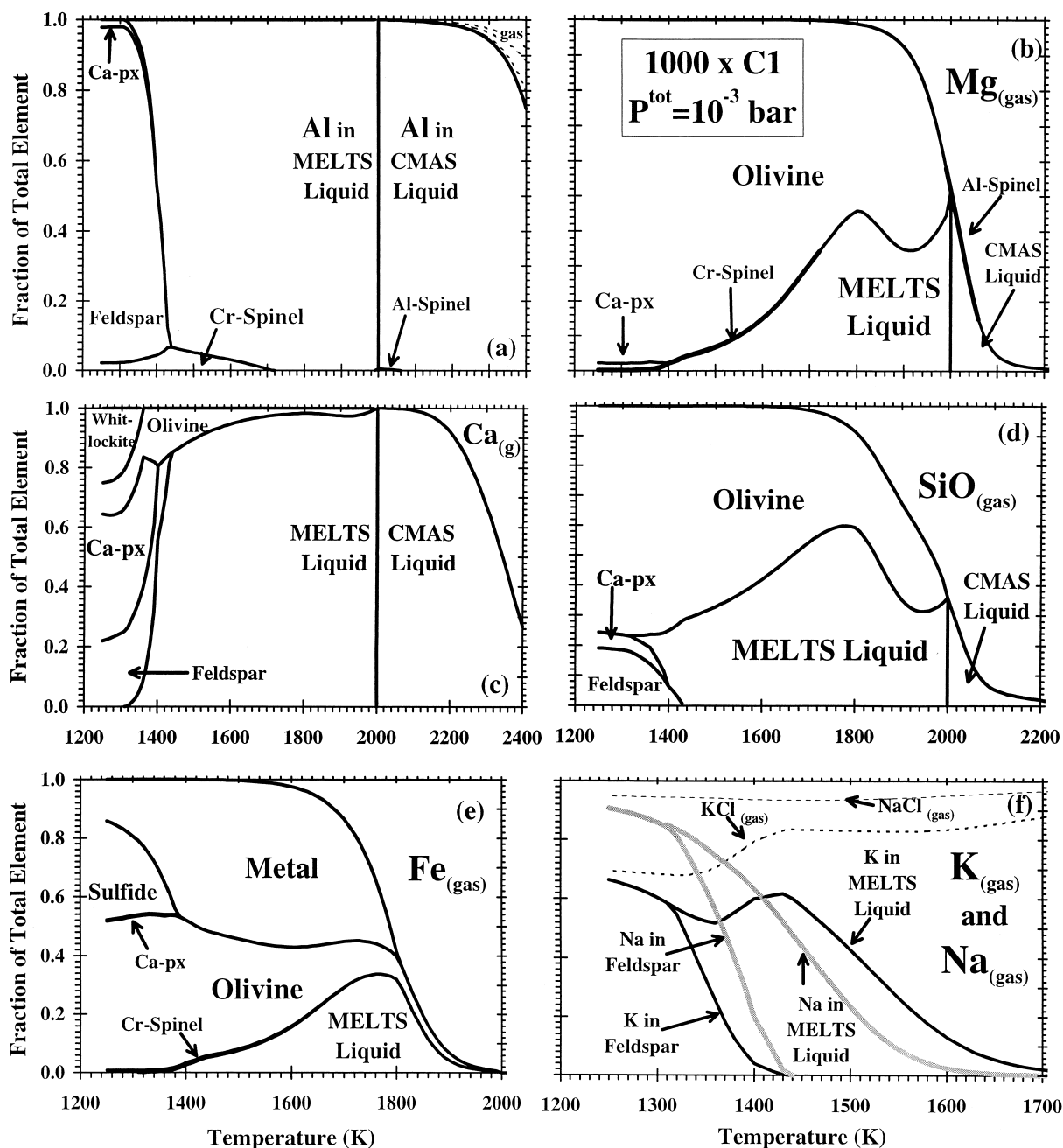
Fig. 6. Distribution of: (a) Al, (b) Mg, (c) Ca, (d) Si, (e) Fe, and (f) Na and K between condensed phases and vapor at a dust enrichment of 100× at $P^{tot} = 10^{-3}$ bar. Note vertical scale change in (e). Al–spinel = spinel with ≤1 wt.% Cr_2O_3; Cr–spinel = spinel with >1 wt.% Cr_2O_3. Other abbreviations as used previously.

total Ti in the system by 1850 K. At 1830 K, gaseous Mg, Fe, and Cr begin to react with the liquid and perovskite to form an Mg-, Al-rich spinel with minor amounts of Cr, Fe, and Ti. By 1810 K, this spinel has molar Fe/Mg and Cr/Al ratios of 3.4×10^{-3} and 1.3×10^{-2}, respectively, and a TiO_2 content of 9.1 wt.%, so much Ti that perovskite disappears at this temperature. With falling temperature, Ti and Mg continue to condense into spinel, and Si and Mg into the liquid. The SiO_2 and MgO contents of the liquid increase, and the $MgAl_2O_4$ component of the spinel dissolves into the liquid. By 1780 K, the liquid reaches ~40 wt.% SiO_2 and ~26% MgO, olivine (0.25 wt.%

FeO, 0.73% CaO) becomes stable and, as discussed above, this triggers the switchover from the CMAS to the MELTS liquid model. At this point, the spinel has molar Fe/Mg and Cr/Al ratios of 3.0×10^{-3} and 2.3×10^{-2}, respectively and, because Ti can now be accommodated by the liquid model, the TiO_2 content of the liquid is 0.8 wt.% and Ti drops to only 0.44 wt.% in the spinel. With falling temperature, most olivine forms by wholesale condensation of Mg and Si from the gas but some by crystallization of the liquid. With the total amount of liquid decreasing slightly, the $MgAl_2O_4$ component of spinel continues to dissolve into it, causing the molar Fe/Mg and Cr/Al

Fig. 7. Distribution of: (a) Al, (b) Mg, (c) Ca, (d) Si, (e) Fe, and (f) Na and K between condensed phases and vapor at a dust enrichment of 1000× at $P^{tot} = 10^{-3}$ bar. Abbreviations as used previously.

ratios in spinel to rise to 9.0×10^{-3} and 6.2×10^{-2}, respectively, just before spinel dissolves completely into the liquid at 1710 K. With falling temperature, the FeO content of olivine increases and its CaO decreases, reaching 0.89 and 0.48%, respectively, at the point where spinel disappears and 1.29% and 0.42%, respectively, at 1690 K, the initial condensation temperature of metallic NiFe. This alloy contains 13.6 wt.% Ni, 0.48% Co, and 0.24% Cr. As the temperature falls, olivine of increasing FeO and decreasing CaO content continues to condense from the gas, Si and Fe continue to condense into the liquid, diluting its MgO, Al_2O_3, and CaO contents, and metal of

decreasing Ni and Co and increasing Cr content continues to condense. At 1620 K, when nearly all the Mg and 80% of the Si are condensed, gaseous SiO begins to react with olivine and liquid to form orthopyroxene, whose initial FeO content is 1.1 wt.%. At this point, olivine contains 1.9 wt.% FeO and 0.23% CaO and the liquid contains 0.59 wt.% TiO_2, 0.23% Cr_2O_3, and 0.30% FeO. At 1600 K, gaseous Cr begins to react with the liquid to form a small amount of Cr–spinel, having molar Fe/Mg and Cr/Al ratios of 0.049 and 2.1, respectively, and a TiO_2 content of 0.26 wt.%. With falling temperature, orthopyroxene of increasing FeO content continues to form by reaction

of gaseous SiO with liquid and with olivine of increasing FeO and CaO contents; all components of the metal alloy continue to condense, resulting in decreasing Ni, Co, and Cr contents; the amount of Cr–spinel continues to increase at the expense of Al_2O_3 in the liquid and gaseous Cr; and the CaO and TiO_2 contents of the liquid increase while its FeO and Cr_2O_3 contents decrease. By 1550 K, 1.8% of the K has condensed into the liquid which contains 0.01 wt.% K_2O. At 1450 K, 99% of the Fe is condensed, and gaseous Na begins to react with the liquid to form plagioclase feldspar containing 1.6 mol% albite. At this point, olivine contains 2.30 wt.% FeO and 0.34% CaO, Cr–spinel has molar Fe/Mg and Cr/Al ratios of 0.053 and 1.43, respectively, and 0.34 wt.% TiO_2, and liquid contains 0.93 wt.% TiO_2, 0.20% Cr_2O_3, 0.19% FeO, 0.06% K_2O, and 0.01% Na_2O. At 1440 K, a diopsidic clinopyroxene begins to cocrystallize with feldspar from the remaining liquid, which reaches 0.15 wt.% K_2O and 0.03% Na_2O before disappearing at 1390 K. With continued cooling, gaseous Na and K react with anorthitic feldspar, increasing its albite and orthoclase contents and displacing Ca which, in turn, reacts with orthopyroxene to form clinopyroxene and olivine. The FeO contents of olivine, orthopyroxene, clinopyroxene, and spinel all increase as metallic Fe becomes oxidized, causing the Ni and Co contents of the alloy to increase even as its Cr content decreases due to reaction with spinel. At 1350 K, gaseous Mn reacts with Ti in the spinel and clinopyroxene to form an oxide solid solution consisting of pyrophanite [$MnTiO_3$] with 9.4 wt.% MgO and 2.6% FeO. At 1300 K, the remaining gaseous Mn begins to condense as MnO. By 1200 K, olivine contains 3.6 wt.% FeO and 0.10% CaO; clinopyroxene contains 1.4% Al_2O_3, 0.62% FeO, 0.25% TiO_2, and 0.27% Na_2O; spinel has molar Fe/Mg and Cr/Al ratios of 0.13 and 5.1, respectively, and a TiO_2 content of 0.59%; and the oxide solid solution contains only 1.3% MgO and 1.6% FeO. At this temperature, Na, K, and Mn are only partially condensed, with 15%, 43%, and 3.5%, respectively, remaining in the vapor.

3.4. Condensation at 1000× and $P^{tot} = 10^{-3}$ Bar

The distributions of Al, Mg, Ca, Si, Fe, and Na and K between condensed phases and vapor are illustrated in Figs. 7a, 7b, 7c, 7d, 7e, and 7f, respectively, for a system enriched 1000× in dust at $P^{tot} = 10^{-3}$ bar. At a dust enrichment of 1000×, a CMAS liquid is already present at 2400 K, into which 75% of the Al and 27% of the Ca have condensed. At 2050 K, gaseous Ti, Mg, Cr, and Fe begin to react with Al_2O_3 in the liquid to form a spinel containing 44.8 wt.% MgO, 39.5% TiO_2, 12.7% Al_2O_3, 1.8% Cr_2O_3, 1.1% FeO, and 0.12% Fe_2O_3. At 1990 K, olivine begins to form primarily by condensation from the gas but some also by crystallization from the liquid, and the switch is made from the CMAS to the MELTS liquid model which, because the latter can accommodate TiO_2, causes the titanian spinel to dissolve into the liquid. The initial olivine contains 0.92 wt.% FeO and 0.23% CaO but, as Fe and Mg condense into it, reaches 10.8% FeO and 0.13% CaO by 1800 K. Over the same temperature range, as Fe and Cr condense into the liquid, the composition of the latter evolves from 0.73 wt.% FeO, 0.39% TiO_2, 0.02% Cr_2O_3, and <0.01% Fe_2O_3 to 24.2% FeO, 0.23% TiO_2, 0.90% Cr_2O_3, and 0.19% Fe_2O_3. Metal alloy containing 20.0 wt.% Ni, 0.70% Co, and 0.09% Cr

begins to condense at 1800 K, and reaches 11.7% Ni, 0.52% Co, and 0.06% Cr by 1720 K. In this temperature range, olivine continues to form at the expense of liquid and reaches 14.3 wt.% FeO and 0.13% CaO, while the liquid composition evolves to 25.9 wt.% FeO, 0.25% TiO_2, 1.22% Cr_2O_3, and 0.16% Fe_2O_3. At 1710 K, a small amount of Cr–spinel begins to form by drawing Al and most of its Cr from the liquid but some of its Cr also from the gas and the metal. Initially, it has molar Fe/Mg and Cr/Al ratios of 0.62 and 3.79, respectively, and contains 1.10 wt.% Fe_2O_3 and 0.27% TiO_2, but varies in composition as it continues to crystallize from the liquid with falling temperature, reaching molar Fe/Mg and Cr/Al ratios of 1.34 and 2.29, respectively, with 1.42 wt.% Fe_2O_3 and 1.07% TiO_2 at 1440 K. Over the same temperature range, the amount of olivine continues to increase with falling temperature, drawing its MgO, SiO_2, and CaO from the liquid. From 1710 to 1560 K the FeO consumed by olivine comes from both liquid and gas but, at 1560 K (the temperature below which <1% of the Fe remains in the gas) oxidation of the metal alloy joins the liquid as a source of the FeO for continued production of olivine. The amount of metal alloy increases with falling temperature from 1710 to 1560 K, as gaseous Fe continues to condense into it, diluting its Ni, Co, and Cr concentrations to 9.3 wt.% Ni, 0.43% Co, and 0.01% Cr at 1560 K. Below 1560 K, however, oxidation of Fe causes the amount of metal to decrease with falling temperature, increasing its Ni and Co contents to 10.0 and 0.46 wt.%, respectively, by 1440 K. Its Cr content continues to decrease due to formation of increasing amounts of Cr–spinel with falling temperature. Olivine contains 21.1 wt.% FeO and 0.24% CaO at 1560 K, and 24.6% FeO and 0.45% CaO at 1440 K. As the amount of liquid decreases with falling temperature, its FeO, Cr_2O_3, and Fe_2O_3 contents progressively decrease, reaching 17.6 wt.%, 0.45% and 0.02%, respectively, at 1560 K and 10.8%, 0.12%, and 0.01% at 1440 K; and its TiO_2, Na_2O, K_2O, and P_2O_5 contents progressively increase, reaching 0.43 wt.%, 0.29%, 0.10%, and <0.01%, respectively, at 1560 K and 0.56%, 2.79%, 0.35%, and 0.20% at 1440 K. At 1480 K, MnO condenses and, at 1430 K, plagioclase containing 34.4 mol% albite and 0.35% orthoclase begins to crystallize from the liquid. As the amount of plagioclase increases with falling temperature, its albite and orthoclase contents also increase. Although the Na required for this is supplied by both gas and liquid, the K is derived only from the liquid, with the proportion of K residing in the vapor actually increasing initially with falling temperature. At 1390 K, a diopside-rich clinopyroxene, containing 4.7 wt.% FeO, 2.3% Al_2O_3, 0.18% Na_2O, 0.36% TiO_2, and 0.09% Fe_2O_3, crystallizes from the liquid. At 1380 K, a pyrophanite-rich oxide solid solution, containing 9.53 wt.% FeO, 1.02% MgO, and 0.52% Fe_2O_3, forms by reaction of gaseous Mn with TiO_2 in the liquid; and gaseous sulfur begins to react with metallic Fe to form pyrrhotite, $Fe_{0.877}S$. The concentrations of Ni and Co in the residual alloy are 11.5 wt.% and 0.53%, respectively, but increase sharply as more pyrrhotite forms with falling temperature, reaching 21.4% and 0.98%, respectively, at 1310 K. At 1350 K, gaseous P reacts with the liquid to form whitlockite. At 1320 K, just before disappearing, the liquid contains 10.1 wt.% Na_2O, 4.52% FeO, 1.34% K_2O, 0.77% P_2O_5, 0.41% TiO_2 and 0.02% Cr_2O_3. At 1260 K, olivine contains 27.3 wt.% FeO and 0.31% CaO; clinopyroxene contains 4.5 wt.% FeO, 1.6%
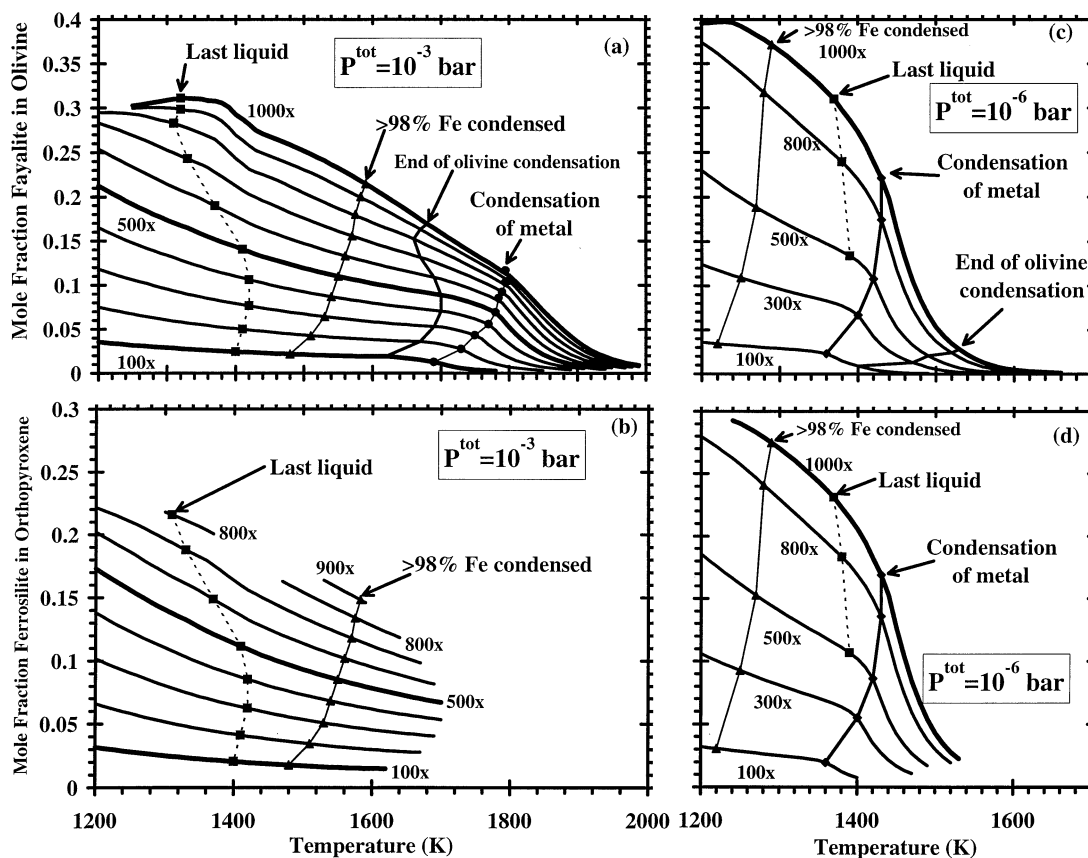
Fig. 8. Mole fraction of iron end-member at 10^{-3} bar in: (a) olivine and (b) orthopyroxene and at 10^{-6} bar in (c) olivine and (d) orthopyroxene as a function of temperature and at dust enrichment factors with integral multiples of 100. Trajectories of the condensation temperature of metallic nickel–iron alloy, the temperature at which direct condensation of olivine ceases, the temperature at which >98% of the total iron is condensed, and the temperature of disappearance of silicate liquid are indicated.

Al_2O_3, 0.33% Na_2O, 0.33% TiO_2, and 0.07% Fe_2O_3; Cr–spinel has molar Fe/Mg and Cr/Al ratios of 2.9 and 7.5, respectively, and contains 2.8 wt.% TiO_2 and 1.5% Fe_2O_3; the pyrophanite-rich solid solution contains 9.2 wt.% FeO, 0.86% MgO, and 0.45% Fe_2O_3; and the metal alloy contains 27.5 wt.% Ni and 1.3% Co. At this point, 97.8% of the P is condensed as whitlockite, 65.1% of the sulfur as pyrrhotite, and 90.0% of the Na and 65.5% of the K as feldspar. The ratio of the proportion of Fe in sulfide to that in metal is 2.2.

3.5. Direct Condensation of Oxidized Iron at High Temperature

The historical motivation behind studying dust enrichment in the solar nebula was to increase the oxygen fugacity so as to produce condensates that are more oxidized than is possible in a gas of solar composition. For example, one of the most perplexing problems for condensation theory is how to produce the observed molar Fe/Fe + Mg ratios that range from 0.2 in olivine and pyroxene in H-group ordinary chondrites, to 0.3 in the LL group, to 0.5 or above in the matrices of some CV3 chondrites. Solar gas is so reducing that all Fe condenses initially as metal. In order to produce FeO-rich silicates, oxidation of this metal, which occurs only at or below ~500 K,

must be followed by diffusion of Fe^{2+} through the crystal structures of pre-existing silicates. This requires equilibration between solids and a low-density gas and efficient diffusion through nearly close-packed silicate structures at temperatures where the rates of these processes are so low that most workers doubt chondritic matter obtained its oxidation state in this way.

The extent to which this problem is alleviated here is illustrated by the fayalite content of olivine and ferrosilite content of orthopyroxene, which are plotted as functions of temperature at various dust enrichments at 10^{-3} bar in Figs. 8a and b and at 10^{-6} bar in Figs. 8c and 8d. In the dust-enriched systems considered in these calculations, the oxygen fugacity is so high that significant amounts of FeO are stable in olivine and pyroxene at very high temperatures, where gas–solid equilibration is much more likely and diffusion rates are expected to be much higher than at the low temperatures where FeO would become stable in a solar gas. In dust-enriched systems, not only does the first-condensing olivine contain significant quantities of FeO, but also, as the temperature falls below the initial condensation temperature of olivine, the equilibrium fayalite content is predicted to increase while additional olivine condenses from the gas. In this temperature interval of direct olivine condensation, Fe^{2+} is incorporated into each olivine grain as it grows directly

from the vapor phase. The assumption of thermodynamic equilibrium requires that all olivine at a given temperature have the same fayalite content, and that is the value computed here. This requires that the relatively fayalite-poor olivine condensed at high temperature must become as fayalite-rich as newly condensing olivine at a lower temperature. If, even at the high temperatures being discussed here, the Fe^{2+} contents of the interiors of the previously formed olivine crystals cannot increase fast enough to maintain equilibrium, the newly condensing olivine at any temperature will have even higher fayalite contents than calculated here. For all dust enrichments considered here at 10^{-6} bar, and for dust enrichments <800× at 10^{-3} bar, we can consider this stage, olivine formation by direct condensation from the gas, to end at the temperature where olivine begins to react with the gas to form orthopyroxene. For dust enrichments ≥800× at 10^{-3} bar, however, direct condensation of olivine ceases at a higher temperature than that for orthopyroxene formation because the fraction of the total Si remaining in the gas becomes very small, <1%. The trajectory of the temperature of cessation of direct olivine condensation is marked on Figs. 8a and 8c. At both values of P^{tot}, a liquid is present which persists to temperatures well below that where orthopyroxene begins forming. The FeO contents of olivine and orthopyroxene continue to rise with falling temperature and, with liquid present, this can occur by equilibration of olivine and orthopyroxene with the liquid. This is a much more kinetically favorable process for forming FeO-rich silicates than equilibration with a low-density gas.

At 10^{-3} bar, X_{Fa} for the first-condensing olivine is only 2.5×10^{-3}, 5.1×10^{-3}, and 9.1×10^{-3} at dust enrichments of 100×, 500×, and 1000×, respectively. At the temperature where olivine condensation ends, however, X_{Fa} has increased to 0.019, 0.088, and 0.164 at dust enrichments of 100×, 500×, and 1000×, respectively, and, at the temperature of disappearance of liquid, X_{Fa} is 0.025, 0.14, and 0.31. At 10^{-6} bar, X_{Fa} is lower in the first-condensing and last-condensing olivine than at 10^{-3} bar and the same dust enrichment, and almost the same at the temperature where the liquid disappears. Below the solidus, continued increase in the FeO content of olivine with decreasing temperature is governed by multiphase equilibrium, which would be impeded not only by slow diffusion of Fe^{2+} into silicates but also by slow solid-state reaction rates between olivine, orthopyroxene, clinopyroxene, and plagioclase, and by slow reaction between gaseous oxidizing agents and metallic iron. If the arbitrary assumption is made that multiphase equilibrium can be maintained to temperatures as low as 1200 K, nebular olivine can be expected to have X_{Fa} of 0.036 and 0.21 at dust enrichments of 100× and 500×, respectively, at 10^{-3} bar, and 0.036, 0.23, and 0.40 at dust enrichments of 100×, 500×, and 1000×, respectively, at 10^{-6} bar. Higher FeO contents require equilibration to lower temperatures under these conditions or condensation at higher dust enrichments.

At a given P^{tot}, the temperature at which gaseous SiO begins to react with olivine to form orthopyroxene increases, reaches a maximum, and finally decreases with progressively increasing dust enrichment. At a dust enrichment of 1000×, there is no orthopyroxene stability field at all at 10^{-3} bar. At relatively low dust enrichments, the orthopyroxene condensation temperature increases with increasing dust enrichment due to the attendant increase in the partial pressure of SiO. Accompanying this,
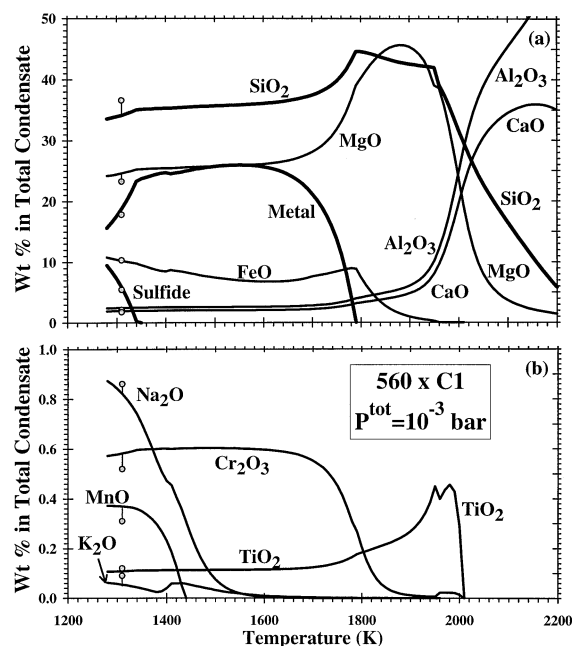

Fig. 9. Concentrations of: (a) major and (b) minor components of the total condensate as a function of temperature at the stated conditions. Filled circles indicate average composition of H-group chondrites.

however, is an increase in the $(FeO + MgO)/SiO_2$ ratio of the silicate fraction of the condensate due to the increase in oxygen fugacity with increasing dust enrichment. This tends to stabilize olivine at the expense of orthopyroxene. A dust/gas ratio is reached beyond which the stabilizing effect on orthopyroxene of the increasing partial pressure of SiO is outweighed by the stabilizing effect on olivine of the increasing $(FeO + MgO)/SiO_2$ ratio. This causes the orthopyroxene field to shrink at the expense of the olivine field with increasing dust/gas ratio, and eventually disappear altogether.

3.6. Bulk Chemical Composition of Condensates

In Figures 9a and 9b, the bulk chemical composition of the total condensate is plotted as a function of temperature at a P^{tot} of 10^{-3} bar and a dust enrichment of 560×. Features of this diagram which are common to condensation at all dust enrichments are the early entry of Al, Ca, and Ti relative to Mg and Si, as well as the relatively late entry of Na, K, and Mn into the condensates. Features specific to condensation at this dust enrichment are the relative proportions of metal, FeO, and sulfide as a function of temperature. This particular dust enrichment was chosen because it yields a single temperature at which the distribution of Fe between metal, sulfide, and silicate matches closely the distribution found in H-group ordinary chondrites and results in a bulk chemical composition very close to the average of those meteorites. For example, at 1310 K the total condensate and, for comparison (brackets), the average H-group chondrite fall from Jarosewich (1990) contain 18.8 (17.8) wt.% Fe + Ni + Co metal, 10.2 (10.3)% FeO, 5.9 (5.4)% FeS, 34.2 (36.6)% SiO_2, and 24.6 (23.3)% MgO. Similarly, at the same P^{tot} and a slightly higher dust enrichment of
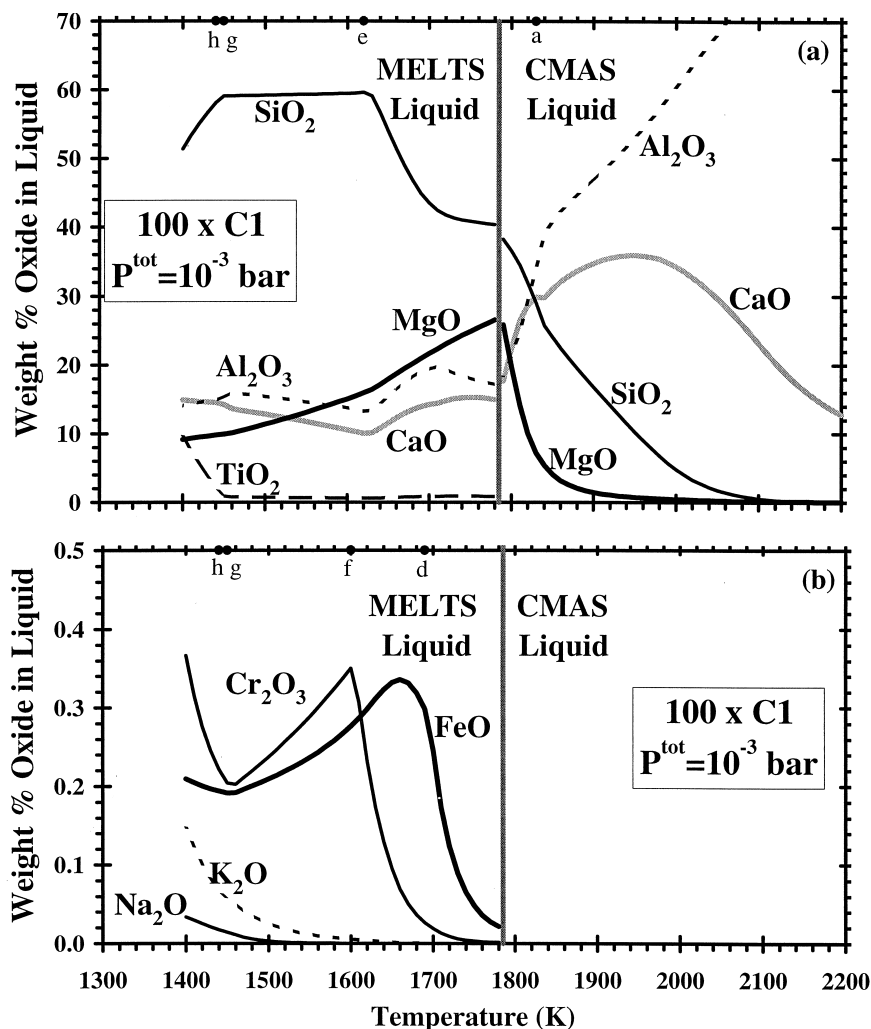
Fig. 10. Compositions of condensate liquids at: (a), (b) 10^{-3} bar and a dust enrichment of 100×; (c), (d) 10^{-3} bar and a dust enrichment of 1000×; and (e), (f) 10^{-6} bar and a dust enrichment of 1000×. In all cases, the vertical line marks the condensation temperature of olivine, where the transition between CMAS and MELTS liquid models is made. In (e) and (f), $Na_2O \leq 0.01$ wt.%. Inflection points are due to the onset of crystallization or disappearance of a coexisting phase, and are labelled as follows: a, spinel in; d, metal in; e, orthopyroxene in; f, Cr–spinel in; g, feldspar in; h, clinopyroxene in; k, rhombohedral oxide in; p, perovskite in; q, clinopyroxene in and liquid out.

675×, a temperature can be found at which the bulk chemical composition of the condensate comes very close to the average composition of L-group chondrite falls from Jarosewich (1990). In the following comparison, sufficient metal of the same composition as that in Jarosewich's average L-group chondrite has been added to his average L-group chondrite bulk composition to yield the same atomic Fe/Si ratio as in H-group chondrites. At 1330 K, the condensate contains 16.8 (16.1) wt.% metal, 12.9 (13.2)% FeO, 5.5 (5.3)% FeS, 34.0 (36.3)% SiO_2, and 24.5 (22.6)% MgO. In both cases, the MgO/SiO_2 ratio of the condensate is higher than in the chondrite due to the fact that the relative abundances of nonvolatile elements in the model system are those of Cl chondrites, which are known to have a higher atomic Mg/Si ratio than ordinary chondrites. Nevertheless, the close correspondence in composition between the predicted condensates and the chondrite averages serves to emphasize the point that the distribution of iron between metal,

silicate, and sulfide in ordinary chondrites could have been established during high-temperature condensation in a dust-enriched system.

3.7. Composition of Silicate Liquid

The temperature variation of the composition of the silicate melt is shown for the cases of 10^{-3} bar and a dust enrichment of 100× in Figures 10a and 10b, 10^{-3} bar and a dust enrichment of 1000× in Figures 10c and 10d, and for 10^{-6} bar and a dust enrichment of 1000× in Figures 10e and 10f. The evolution of the liquid composition is similar in all cases, but some exceptions are noteworthy. Because Al is more refractory than Ca, the Al_2O_3 content of the initial liquid is very high but falls with decreasing temperature due to dilution by CaO which condenses more gradually with falling temperature. Similarly, at lower temperatures, incipient condensation of more volatile
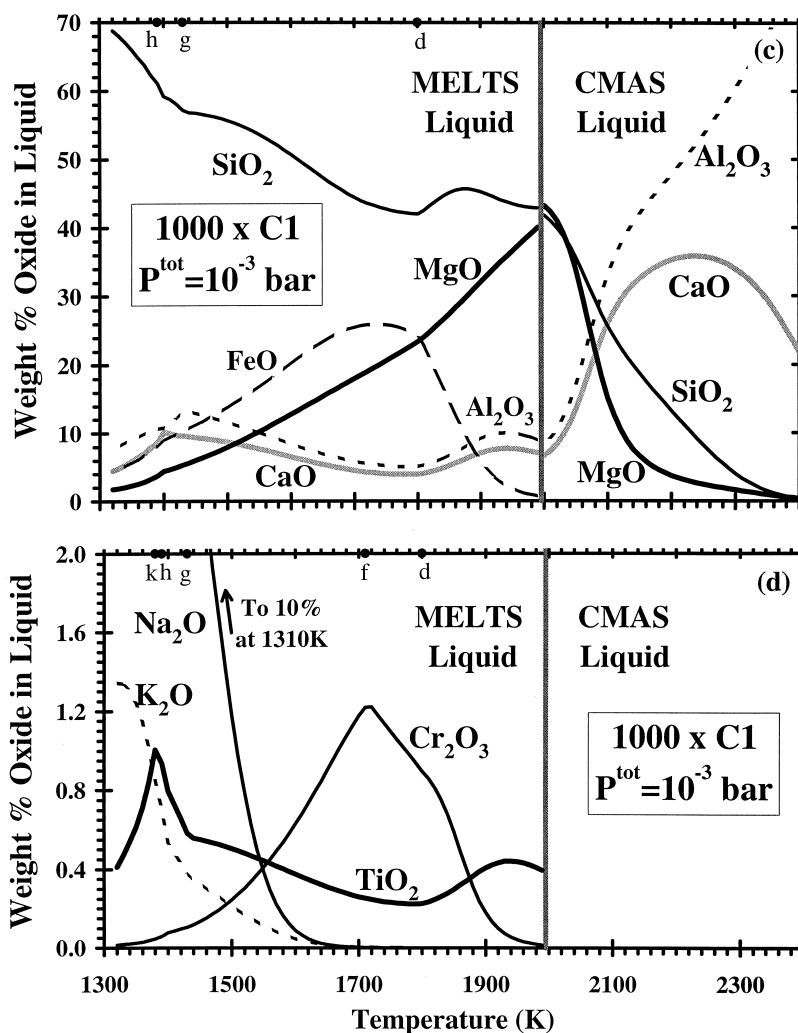
Fig. 10 (Continued)

Si and Mg into the liquid causes the concentrations of SiO_2 and MgO to increase, diluting both Al_2O_3 and CaO. Comparing Figs. 10a and 10c it is seen that for liquids that form at higher temperatures than olivine, similar liquid compositions are stable at temperatures 300 K higher when the dust enrichment is increased by a factor of 10 at 10^{-3} bar. Similarly, comparing Figs. 10c and 10e reveals that liquids of similar composition form about 400 K higher when P^{tot} is increased by a factor of 1000 at a dust enrichment of $1000\times$. Note however that at the condensation temperatures of olivine, liquid compositions are quite different from one another at different combinations of P^{tot} and dust enrichment. For example, the concentrations of MgO and SiO_2 in the liquid at a dust enrichment of $1000\times$ are almost the same where olivine condenses at 10^{-3} bar (Fig. 10c) but the SiO_2 content is more than double that of MgO at 10^{-6} bar (Fig. 10e). One way of understanding this is by considering the fact that the solubility of olivine in a melt of a given composition is quite different at temperatures hundreds of degrees apart.

Below the condensation temperature of olivine, the main difference in major element trends of the liquid at different combinations of P^{tot} and dust enrichment, aside from those of

FeO and alkalis, is the failure of the SiO_2 concentration to level off with falling temperature at a dust enrichment of $1000\times$ at 10^{-3} bar (Fig. 10c) as it does at a dust enrichment of $100\times$ at 10^{-3} bar (Fig. 10a) and $1000\times$ at 10^{-6} bar (Fig. 10e). This is entirely due to the absence of orthopyroxene from the crystalline assemblage in equilibrium with the liquid at a dust enrichment of $1000\times$ at 10^{-3} bar. It is the condensation of this phase that triggers the flattening of the SiO_2 curve under the other sets of conditions. Of the three cases shown, it is at a dust enrichment of $1000\times$ and 10^{-3} bar where the Cr_2O_3 content of the liquid is highest, climbing to 1.2 wt.% with falling temperature, and then declining after Cr–spinel becomes stable at 1710 K (Fig. 10d). At a dust enrichment of $100\times$ at 10^{-3} bar, this phase becomes stable at 1600 K, before the Cr_2O_3 content of the liquid reaches 0.36 wt.% (Fig. 10b). At a dust enrichment of $1000\times$ at 10^{-6} bar, Cr–spinel coexists with the MELTS liquid over its entire stability range, preventing its Cr_2O_3 content from exceeding 0.28 wt.% (Fig. 10f). As the amount of liquid becomes vanishingly small during near-solidus crystallization of clinopyroxene and plagioclase, concentrations of TiO_2 are seen to build up in the last dregs of liquid. Only at a dust enrichment of $1000\times$ at 10^{-3} bar does this trend reverse itself. This is due
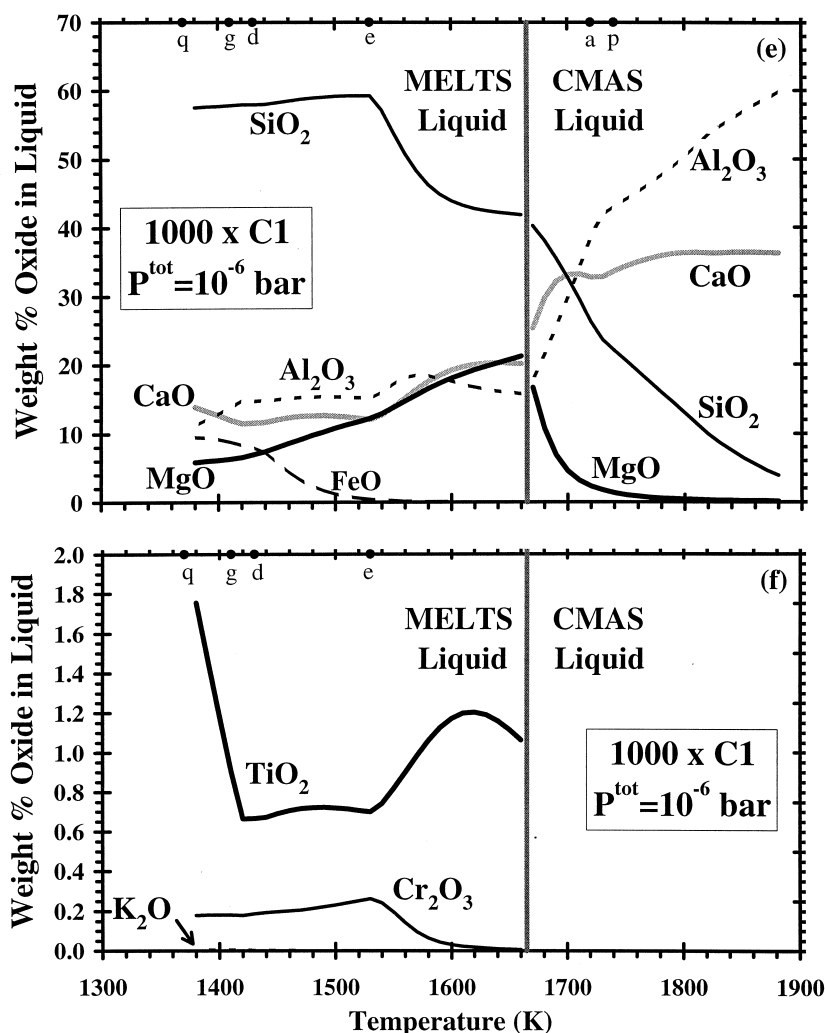
Fig. 10. (Continued)

to stabilization of a pyrophanite-rich solid solution at a temperature above that for the disappearance of liquid. As seen by comparing Figs. 10b, 10d, and 10f, alkali contents of the liquid increase both with increasing P^{tot} and with increasing dust enrichment because the partial pressures of sodium and potassium increase with both parameters. As a result, Na_2O and K_2O concentrations in the liquid are negligible at 10^{-6} bar, even at a dust enrichment of $1000\times$. In the other cases shown, Na_2O and K_2O concentrations rise above negligible levels only within 100 to 200 K of the temperature of disappearance of liquid, reaching maxima of 10.1 and 1.3 wt.%, respectively, at 10^{-3} bar and a dust enrichment of $1000\times$. At a dust enrichment of $1000\times$, the FeO content of the liquid at 10^{-3} bar is higher than at 10^{-6} bar at most temperatures (Figs. 10c and 10e), considerably so at some temperatures. Because f_{O_2} is only weakly dependent on P^{tot} at 1500 to 1600 K, the higher FeO content of the liquid is due simply to the higher P_{Fe} at higher P^{tot}, which causes a greater proportion of the iron to be condensed at any given temperature.

In most cases, the liquid disappears in the temperature interval 1370 to 1400 K, the approximate location of the peridotite solidus at 1 bar (see Table 5). An exception to this general rule

is found in Table 8 for the case of a dust enrichment of $1000\times$ at 10^{-3} bar, where the liquid persists to 1310 K. At the same P^{tot} and a dust enrichment of $500\times$, the liquid disappears at a significantly higher temperature, 1400 K. Similarly, at the same dust enrichment ($1000\times$) and lower P^{tot} (10^{-6} bar) the liquid also disappears at a much higher temperature (1370 K). At 10^{-3} bar, the reason for the different solidification temperatures at the different dust enrichments is evident from a comparison of the liquid compositions in the two cases at 1410 K, the last temperature step before the liquid disappears at a dust enrichment of $500\times$. At this temperature, the liquid at the lower dust enrichment contains slightly less Na_2O (2.67 wt.%) and much less FeO (3.26%) than the liquid at the higher dust enrichment (3.81% and 9.46%, respectively) and high concentrations of both of these oxides are known to depress solidus temperatures. At a dust enrichment of $1000\times$, the reason for the different solidification temperatures at the different total pressures is found in the different liquid compositions at 1380 K, the last temperature step before the liquid disappears at 10^{-6} bar. Although the FeO content of the liquid is slightly lower at 10^{-3} than at 10^{-6} bar, 7.54 vs. 9.51 wt.%, the Na_2O concentration is much higher at 10^{-3} than at 10^{-6} bar, 5.89 vs. <0.01
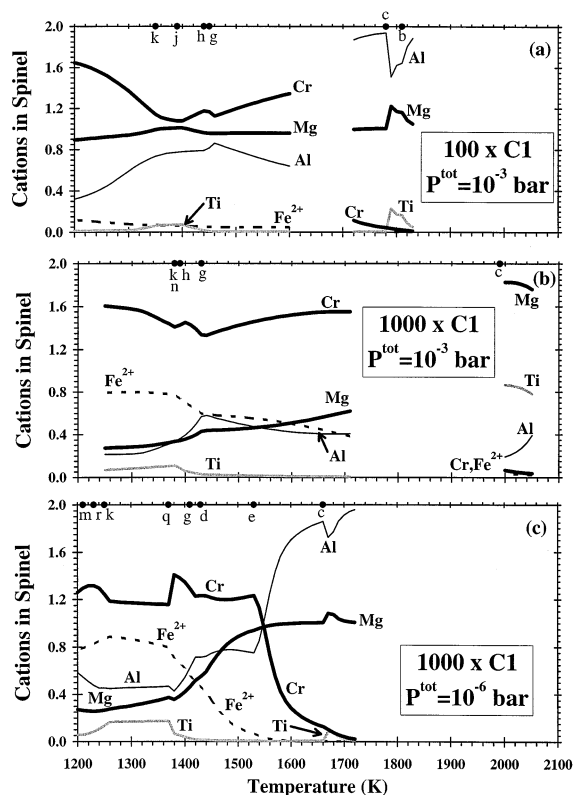
Fig. 11. Composition of spinel as a function of temperature at: (a) $P^{tot} = 10^{-3}$ bar and a dust enrichment of 100×; (b) $P^{tot} = 10^{-3}$ bar and a dust enrichment of 1000×; and (c) $P^{tot} = 10^{-6}$ bar and a dust enrichment of 1000×. Inflection points labelled as in Fig. 10, plus: b, perovskite out; c, olivine in; j, liquid out; m, MnO in; n, pyrrhotite in; r, orthopyroxene out.

wt.%. This is because the partial pressure of Na is more than a factor of 200 higher at 1380 K at 10^{-3} bar than at 10^{-6} bar. Furthermore, because Na continues to condense into the liquid in this temperature range, the lower the temperature to which the liquid persists, the higher its Na_2O content becomes, and this further lowers the ultimate temperature of its disappearance.

3.8. Composition of Spinel

The numbers of cations in spinel per four oxygen atoms are plotted as a function of temperature at dust enrichments of 100× and 1000× at 10^{-3} bar in Figures 11a and 11b, respectively, and 1000× at 10^{-6} bar in Figure 11c. In all cases, the highest temperature spinel forms by reaction of gaseous Mg with TiO_2 in perovskite and Al_2O_3 in the CMAS liquid, except at 1000× and 10^{-3} bar, where all Ti is from the gas. In this spinel, the Ti cations first increase with falling temperature as perovskite and/or gaseous Ti are consumed and then decrease sharply when the MELTS liquid, which can accommodate Ti, becomes stable. Both stages proceed in accordance with the coupled substitution of $Mg^{2+} + Ti^{4+} = 2Al^{3+}$, and are accompanied by steadily rising numbers of Fe and Cr cations which are condensing from the gas. As discussed previously, the high Ti contents of these spinels and possibly even their

existence, may be artifacts of the inability of the CMAS liquid to accommodate Ti. The incoming of the MELTS liquid causes the very Ti-rich spinel at 1000× and 10^{-3} bar to dissolve suddenly, and the less Ti-rich spinel at 100× and 10^{-3} bar to dissolve gradually before disappearing. The even lower Ti spinel at 1000× and 10^{-6} bar continues to crystallize with falling temperature, gradually becoming first more Cr-rich and then more Fe-rich. As shown in Fig. 11c, the Cr/Al ratio levels off below 1390 K, as formation of spinel continues by reaction of gaseous Cr with Al_2O_3 in the liquid. When spinel re-forms in the two cases at 10^{-3} bar, its Cr/Al ratio falls, as the spinel draws down Al_2O_3 from the liquid while deriving its Cr from the metal alloy and the gas at 100×, and from the metal alloy and the liquid at 1000×. In all three cases, these trends are interrupted by plagioclase formation, which draws Al_2O_3 from the $MgAl_2O_4$ component of the spinel, increasing the Cr/Al ratio and decreasing the amount of spinel. Plagioclase formation also causes an increase in the rate of increase of the number of Ti cations in the spinel with decreasing temperature, accompanied by an increase in the number of Mg and/or Fe ions in accordance with the above coupled substitution. At lower temperature, the number of Ti ions in the spinel begins to decrease with decreasing temperature due to extraction of Ti into pyrophanite or, at 100× and 10^{-3} bar, clinopyroxene.

3.9. Composition of Clinopyroxene

The concentrations of FeO, Al_2O_3, and TiO_2 in clinopyroxene are plotted as a function of temperature at 10^{-3} bar and dust enrichments of 100× and 1000×, and at 10^{-6} bar and 1000× in Figures 12a, 12b, and 12c, respectively. The amount of clinopyroxene increases with falling temperature in all three cases due either to crystallization from the liquid or, after liquid is exhausted, to reactions among plagioclase, orthopyroxene, and olivine, as can be seen in Figs. 6 and 7 for the cases at 10^{-3} bar. The proportion of the total Fe accounted for by clinopyroxene increases with falling temperature as metal is oxidized, but the concentration of FeO may rise or fall depending on the relative rates of formation of Mg and Fe end-members. Similarly, the proportions of the total Al and Ti accounted for by clinopyroxene increase with falling temperature as this phase crystallizes from the liquid in the cases at 10^{-3} bar, but the concentrations of Al_2O_3 and TiO_2 may increase or decrease with falling temperature due to the relative formation rates of the different pyroxene end-members. At 10^{-3} bar and 100× and at 10^{-6} bar and 1000×, a temperature is reached below which the Al_2O_3 and TiO_2 concentrations begin to fall with decreasing temperature, as plagioclase begins to draw its Al_2O_3, and pyrophanite its TiO_2, from clinopyroxene.

3.10. Composition of Feldspar

The mole fractions of albite and orthoclase in feldspar are plotted as functions of temperature at 10^{-3} bar and dust enrichments of 100× and 1000× in Figure 13. The amount of feldspar and its albite and orthoclase contents increase steadily with decreasing temperature in both cases. Above the temperature of disappearance of liquid, feldspar draws its Na from both liquid and gas, but its K from the liquid only. Below this temperature, Na and K continue to condense from the gas into
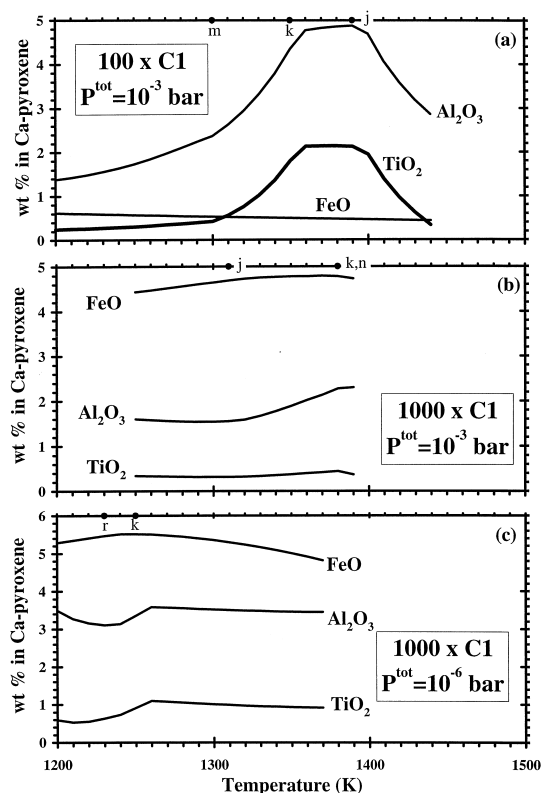
Fig. 12. Composition of Ca-rich clinopyroxene as a function of temperature at: (a) $P^{tot} = 10^{-3}$ bar and a dust enrichment of $100\times$; (b) $P^{tot} = 10^{-3}$ bar and a dust enrichment of $1000\times$; and (c) $P^{tot} = 10^{-6}$ bar and a dust enrichment of $1000\times$. Inflection points as previously labelled.

feldspar, increasing their concentrations in feldspar with decreasing temperature. At 10^{-6} bar and dust enrichments of $100\times$ and $1000\times$, K contents of feldspar are vanishingly small down to the last temperature step of the computations shown in Table 7. This is also true for Na at $100\times$, but X_{Ab} at $1000\times$ rises to 0.1 at 1200 K.
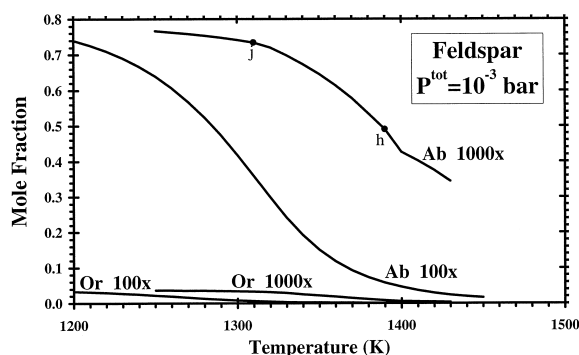
Fig. 13. Mole fractions of albite (Ab) and orthoclase (Or) in feldspar as a function of temperature at $P^{tot} = 10^{-3}$ bar and a dust enrichment of $100\times$ and $1000\times$. Inflection points as previously labelled.
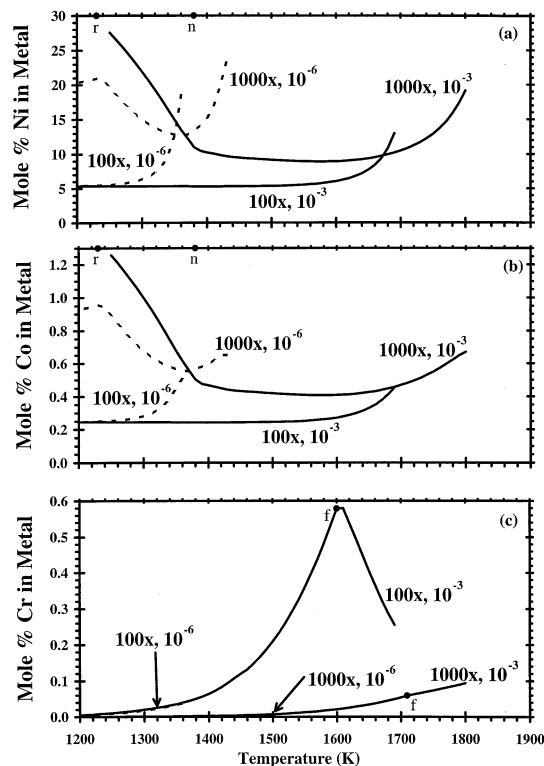
Fig. 14. Mole % of: (a) Ni; (b) Co; and (c) Cr in metallic nickel–iron alloy as a function of temperature at the stated conditions. Inflection points as previously labelled.

3.11. Composition of Metallic Nickel–Iron

The concentrations of Ni, Co, and Cr in the metallic nickel–iron alloy at various combinations of P^{tot} and dust enrichment are shown in Figs. 14a, 14b, and 14c, respectively. Under all conditions shown, Ni and Co are slightly more refractory and have slightly steeper condensation curves than Fe. This leads to high concentrations of Ni and Co in the first-condensing alloys, steadily declining concentrations of Ni and Co with falling temperature as condensation of slightly less refractory Fe dilutes the previously condensed Ni and Co, and finally a leveling off of the Ni and Co contents when all three elements are totally condensed. At still lower temperatures in the more oxidizing cases, $1000\times$ at 10^{-3} and 10^{-6} bar, Ni and Co contents begin to rise very gradually with falling temperature due to oxidation of the Fe component of the alloy. At 1380 K at $1000\times$ and 10^{-3} bar, the Ni and Co contents of the alloy begin to rise very sharply with falling temperature due to reaction of gaseous sulfur with the Fe component of the alloy to form pyrrhotite. Under oxidizing conditions, Cr is slightly more refractory than Fe and, like Ni and Co, falls steadily in concentration with falling temperature. Under more reducing conditions, however, the behavior of Cr is completely different. At $100\times$ and 10^{-3} bar, Cr is slightly less refractory than Fe, its concentration in the metal increases sharply with falling temperature in the high-temperature alloys, and only reverses itself below the formation temperature of Cr–spinel, which extracts Cr from the metal alloy. The increase in Cr content with falling temperature is not seen at $100\times$ and 10^{-6} bar because most of the Cr has
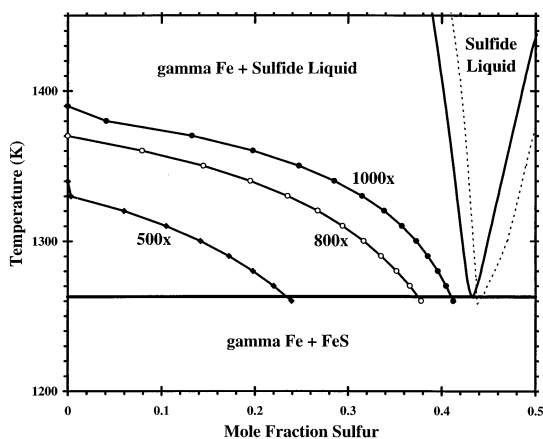
Fig. 15. Bulk chemical compositions of metallic nickel–iron + pyrrhotite condensate assemblages predicted at $P^{tot} = 10^{-3}$ bar and the stated dust enrichments, projected onto the liquid-crystal phase relations of the Fe-rich portion of the Fe–S binary system. Dashed curves show projections of phase boundaries when 7 mol % Ni is present.

already condensed as Cr–spinel at a higher temperature than that where the metal alloy begins to condense. While high Si concentrations in metallic nickel–iron alloys can result from condensation from gases more reducing than a gas of solar composition, X_{Si} is always $<10^{-4}$ in the systems considered in this work.

3.12. Metal–Sulfide Condensate Assemblages

Because of the high concentration of sulfur in dust of Cl composition, enrichment in such dust leads to much higher f_{S_2} and permits sulfide phases to condense at higher temperatures at a given P^{tot} than in a gas of solar composition. Inspection of Table 7 reveals that no sulfide phase becomes stable above the last temperature step of the calculations at any of the dust enrichments shown at 10^{-6} bar, but that at 10^{-3} bar pyrrhotite ($Fe_{0.877}S$) joins metallic nickel–iron as a stable condensate at 1330 and 1380 K at dust enrichments of 500× and 1000×, respectively. These temperatures are higher than minimum melting temperatures in the Ni-poor part of the Fe–Ni–S system but, since our computer program does not contain a thermodynamic model for Fe–Ni–S liquids, it would be unable to predict their existence even if they were more stable than the metal + pyrrhotite assemblages that are predicted. In order to see if sulfide liquids are more stable than the predicted assemblages, the relative atom proportions of Fe and S were calculated for the metallic nickel–iron + pyrrhotite assemblage predicted at each temperature step for dust enrichments of 500×, 800×, and 1000× at 10^{-3} bar, and are plotted on a portion of the liquid-crystal phase relations in the Fe–S binary (Chuang et al., 1986a) in Figure 15. The dashed curves in this figure are the phase boundaries that result from addition of 7% Ni to the system, taken from the work of Hsieh et al. (1982), projected onto the Fe–S plane. Under all conditions, the trajectory of the condensate compositions initially falls vertically along the left margin of the diagram until the temperature of pyrrhotite formation is reached. Below this, the trajectories extend to the right and downward, well above the eutectic temperature of

1262 K and well within the field of γ–iron + Fe–S liquid. The solid assemblage of metallic nickel–iron + pyrrhotite predicted by our thermodynamic model to condense under these conditions is thus seen to form at temperatures where it is actually metastable relative to metallic iron + Fe–S liquid. Nickel, cobalt, and chromium are also predicted to condense into the metal alloy, but the amounts of Co and Cr are quite small and the phase relations are seen to change very little with the addition of 7% Ni, a fairly representative concentration in these condensate assemblages. We conclude that, at these relatively high total pressures and dust enrichments, direct condensation of iron–sulfide liquids will occur. Furthermore, because the liquid-bearing assemblage obviously has a lower Gibbs free energy than the predicted assemblage, the temperature of appearance of sulfide liquid will actually be higher than the condensation temperature of pyrrhotite. Recall that the silicate liquid in the 500× case solidifies at 1400 K, which is well above the minimum condensation temperature of sulfide liquid, but that the silicate liquid at 1000× does not solidify until 1310 K, almost 100 K below the minimum condensation temperature of sulfide liquid in this case. This means that, at the highest dust enrichment factors at high P^{tot}, condensation of coexisting silicate and sulfide liquids occurs, assuming they are not miscible.

4. DISCUSSION

4.1. Stability of Silicate Liquid in Solar Gas

The calculations show that no liquids are stable in a gas of solar composition, even at a total pressure as high as 10^{-3} bar. Any liquids formed by the partial or complete melting of agglomerated solids (Whipple, 1966; Lofgren, 1996) would therefore be highly unstable with respect to partial evaporation in a solar nebula of canonical composition, and would become even more unstable with decreasing pressure. Such liquids would lose FeO and alkali metals most readily, followed by Mg and Si, then Ca and Al with increasing temperature.

Experimentally determined evaporation rates of Na_2O from liquids of chondrule composition (Radomsky and Hewins, 1990; Tsuchiyama et al., 1981; Yu and Hewins, 1998) show that Na loss is faster at lower total pressures and lower f_{O_2}. However, Lewis et al. (1993) showed that sodium loss in alkali olivine basalt melt droplets (3.05 wt.% Na_2O) was nearly attenuated upon heating above 1600 K at $P^{tot} = 1$ bar, at the iron–wüstite buffer in a CO/CO_2 + NaCl vapor with $P_{Na} > 4 \times 10^{-6}$ atm. The present calculations show that these conditions are roughly equivalent to a Cl dust enrichment factor well in excess of 1000× at 10^{-3} bar. Lewis et al. (1993), based on their experiments and following Wood (1984), suggested chondrule formation in 'clumps' where the local partial pressures of condensable elements and oxygen were enhanced by volatilization of chondrule precursor material. The phase diagrams presented above provide the rigorous thermochemical basis for concluding that such a mechanism would indeed stabilize liquids in the solar nebula and reduce or eliminate the driving force for volatilization of Na and other elements from chondrule-like liquids.
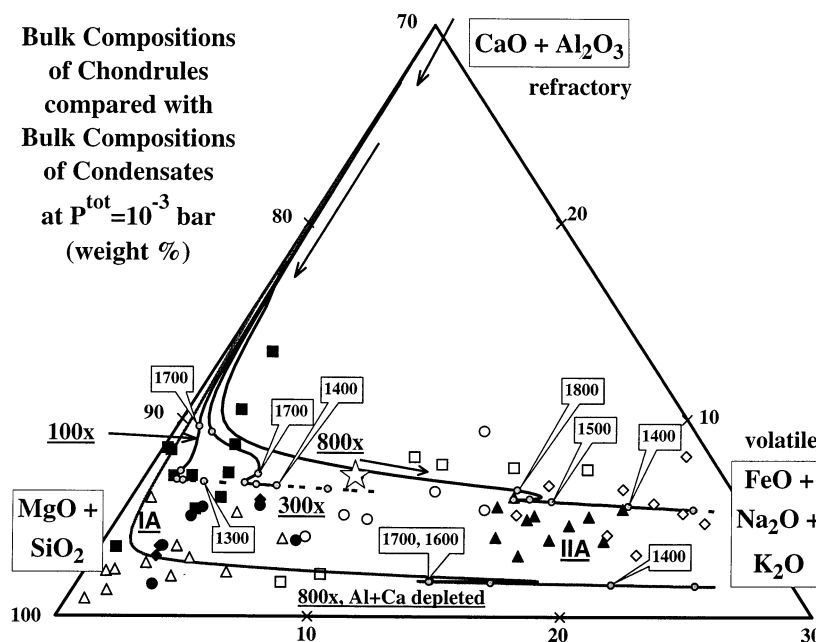
Fig. 16. Bulk compositions of chondrules, and bulk compositions of condensed oxides at 10^{-3} bar. Data: filled squares = type IA (Jones and Scott, 1989); filled diamonds = type IB (Jones, 1994); filled circles = type IAB (Jones, 1994); filled triangles = type IIA (Jones, 1990); open squares = type IIB (Jones, 1996); open circles = H3 (Lux et al., 1981); open triangles = CM and CO (Rubin and Wasson, 1986); open diamonds = Manych L3 (Dodd, 1978). Circles on each path correspond to compositions at 1800, 1700, 1600, 1500, 1400, and 1300 K with increasing FeO + Na$_2$O. Dashed extensions of paths are subsolidus compositions to 1200 K for 100× and 300× and to 1250 K for 800×. Star represents the bulk composition of peridotite KLB-1 (Takahashi, 1986).

4.2. Chondrules in Dust-enriched Systems

Is there some pressure and dust enrichment at which the temperature variation of the bulk composition of the condensed matter, exclusive of metal, resembles the composition range of chondrules? For example, are chondrules the quenched droplets of the solid + liquid assemblages that formed by equilibrium condensation at various temperatures? In Figure 16, chondrule compositions spanning the common composition range are plotted in the forsterite-rich corner of the ternary (CaO + Al$_2$O$_3$)–(MgO + SiO$_2$)–(FeO + Na$_2$O + K$_2$O). This perspective is useful because the apices correspond to groups of oxides which condense in distinct temperature ranges, and these seven oxides constitute the bulk of chondritic material. Superposed on these chondrule compositions are paths representative of the trajectories of bulk oxide condensates, exclusive of metal, with decreasing temperature. Each of the condensation paths sweeps down from the CaO + Al$_2$O$_3$ apex toward the field occupied by type IA chondrules (Jones and Scott, 1989), close to the MgO + SiO$_2$ corner. Note that no single path for a particular combination of P^{tot} and dust enrichment will be able to account for all of the chondrule compositions plotted. Of the cases shown, only the one at the highest dust enrichment, 800×, is oxidizing enough to make sufficient FeO at high temperature that the condensation trajectory passes through the field of type IIA (Jones, 1990) chondrules at temperatures above that where dust and gas could be expected to equilibrate, i.e., ~1200 K. This case is so oxidizing, however, that significant FeO condenses before complete condensation of MgO and SiO$_2$, causing the trajectory to peel away from the (CaO + Al$_2$O$_3$)–

(MgO + SiO$_2$) join before reaching the MgO + SiO$_2$ corner and thus only to graze the top of the field of type IA chondrules. The condensation paths at lower dust enrichments (100× and 300×) are seen to penetrate the type IA field only slightly more, missing the vast majority of the data points in it as well as the type IIA field. Similar composition trajectories to these are obtained at $P^{tot} < 10^{-3}$ bar but, at a given dust enrichment, the temperatures at which the trajectories reach high FeO + alkali contents become progressively lower with decreasing P^{tot}. Sequestration of high-temperature, Ca-, Al-rich condensates could cause the condensation path of the remaining system at a particular P^{tot} and dust enrichment to pass through the middle of the field of type IA chondrules, but such a path would then graze only the bottom of the field of type IIA chondrules. An example of such a path is shown in Fig. 16 for the case of condensation of a system having a dust enrichment of 800× but from which 72% of the Al$_2$O$_3$ and CaO have been removed. Given the wide range of CaO + Al$_2$O$_3$ contents of the chondrules in Fig. 16, it is conceivable that a family of condensation curves corresponding to a single P^{tot} and a high dust enrichment but variable amounts of sequestration of high-temperature condensates could account for the observed data. Although such an appeal to a multitude of adjustable parameters appears to satisfy the data, the separate roles of FeO and alkalies are not addressed in Figure 16.

The FeO and Na$_2$O contents of the same chondrules shown in Figure 16 are illustrated in Figure 17. Representative oxide bulk compositions for condensation paths at 100×, 300×, 500×, and 800× dust enrichment (the latter with and without
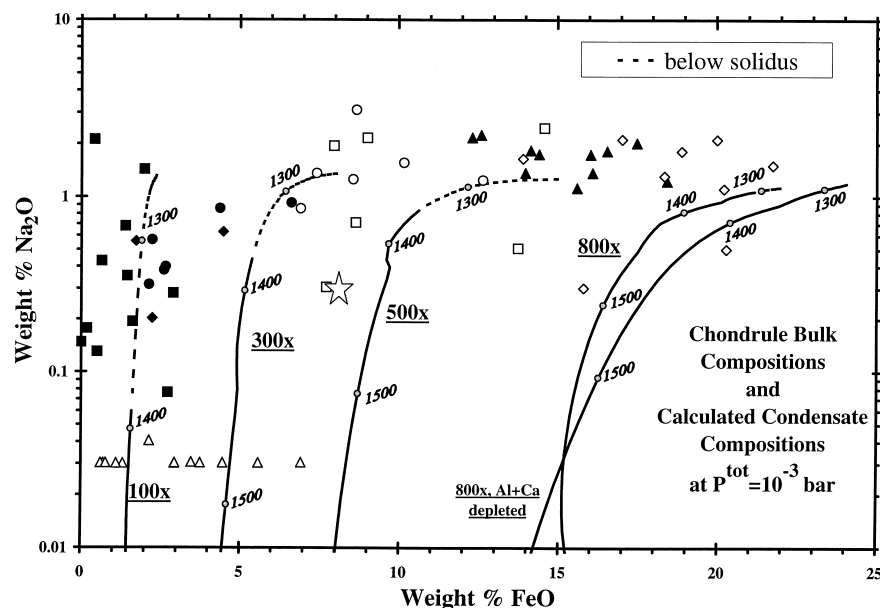
Fig. 17. Sodium and iron oxide contents of the chondrules of Fig. 16 and of KLB-1, with representative paths of bulk oxide condensates. Compositions reported as ≤0.03% Na₂O are plotted at 0.03%.

removal of 72% of the Al_2O_3 and CaO) at 10^{-3} bar are superposed on Fig. 17, with the subsolidus portions dashed. The FeO contents of the calculated condensate assemblages at high dust enrichments reach the levels found in chondrules at high temperatures, but Na_2O contents only approach the levels found in Na-rich chondrules near the solidus of silicate liquid. The compositions of the chondrules richest in both Na_2O and FeO, which include the type IIA and IIB chondrules of Jones (1990; 1996) and many of those reported by Dodd (1978), are more Na_2O-rich than compositions on any of the equilibrium condensation paths calculated under the conditions investigated here. This result precludes formation of these particular chondrules by representative sampling of equilibrium condensate assemblages from dust-enriched systems at specific temperatures, either by quenching and isolating primary condensates or by isochemical melting and quenching of such samples at $P^{tot} \leq 10^{-3}$ bar and dust enrichments ≤1000×. Dust enrichment factors of >800× are not required, however, to produce the iron contents observed in most chondrules. If the FeO contents of chondrules *did* result from the formation and isolation of their precursors in a dust-enriched environment, their Na contents may have resulted from some secondary, as yet unspecified process.

Evidence for only limited intracrystal and liquid-crystal equilibrium in chondrules includes the presence of grains interpreted to be relict olivine and/or pyroxene (Steele, 1986) and chemical zoning in phenocrysts of porphyritic chondrules (Simon and Haggerty, 1979; Jones and Scott, 1989). Because diffusion of major elements in silicate liquids is generally much faster than through crystals, the liquid is likely to have been the last phase to have even partially equilibrated with ambient vapor, and the glass is thus the most likely phase to have preserved a record of the temperature, pressure, and composition of the vapor. In fact, radial chemical zonation in mesostasis of unequilibrated chondrules, particularly with respect to Na_2O

(Ikeda and Kimura, 1985; DeHart et al., 1988; Grossman et al., 1997) suggests that some chondrules underwent only partial equilibration at a late stage in their formation, possibly with surrounding gas. Are there conditions for which the liquids in equilibrium with dust-enriched vapor have the same compositions as the glass found in chondrules? Plotted in Figure 18 are the compositions of the mesostasis from most of the chondrules whose bulk compositions are illustrated in the previous two figures. The axes of Fig. 18 are the same as those of Figure 16, and the composition trajectories for the liquid fraction of the condensates at two dust enrichments are superposed on Figure 18, starting at the temperature where olivine first condenses, and the transition from CMAS to MELTS liquid models occurs. The calculated liquids move away from forsterite toward the CaO + Al_2O_3 apex, then begin to become enriched in iron. Once past the peak in iron content, the paths differ in trajectory, due to differences in the proportions of crystallizing olivine and orthopyroxene, and liquid. Continuing olivine and pyroxene crystallization drives the liquid trajectory steeply away from the MgO + SiO_2 corner, causing CaO and Al_2O_3 concentrations to rise in the liquid until feldspar and pyroxene crystallize, very near the solidus, driving CaO and Al_2O_3 downward again.

The liquid paths in Figure 18 suggest that chondrule glasses with high FeO + alkali oxide contents could have equilibrated with a highly dust-enriched gas at 10^{-3} bar. The glass compositions observed in type IA chondrules, however, contain much less MgO + SiO_2 than any FeO- or alkali-bearing liquids in equilibrium with dust-enriched vapor. In these particular chondrules, it is mostly Na_2O content which pulls the liquid composition off the CMAS join, into the interior of the triangle. This can be seen in Figure 19, which shows glass compositions of the same chondrules, with paths of liquid composition for four dust enrichment factors superposed. Type IA chondrules fall closest to the y-axis. In the case of 1000× enrichment at 10^{-3} bar, the FeO contents of calculated liquids increase to
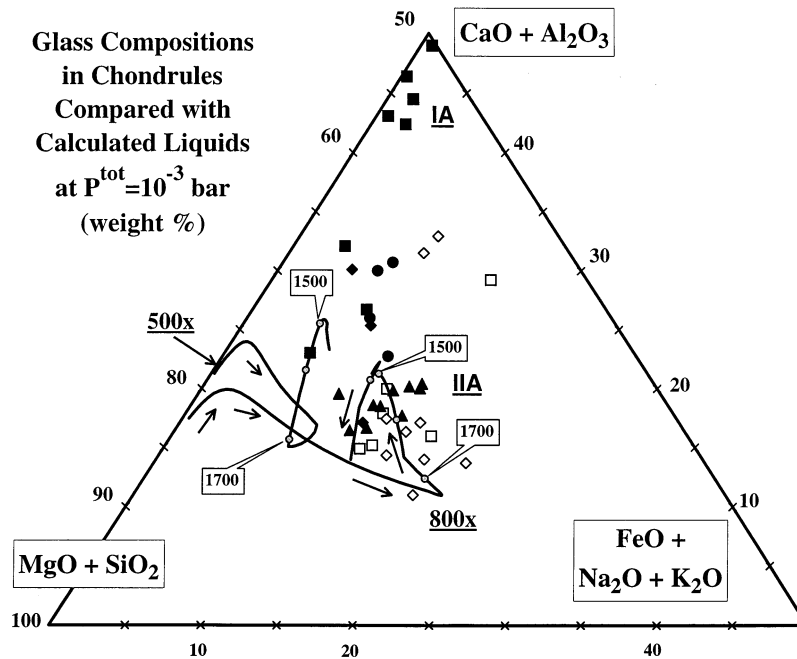
Fig. 18. Glass compositions in chondrules, with paths of condensate liquids for 500 and 800× Cl dust enrichment, from below the appearance temperatures of olivine to their solidi. Symbols for chondrule data as in Fig. 16. Grey circles on each path mark 100° decrements starting at 1700 K.

>25 wt.% while Na_2O < 0.1 wt.%, then decrease with decreasing temperature. Past the peak in FeO content, Na begins to condense into liquids, and Na_2O concentrations increase steeply near the solidus, at which points the curves in Fig. 19 terminate. Prior to Na condensation, P_{Na} is ~2.7 × 10^{-6} bar at a dust enrichment of 1000×, almost three times higher than that at 300×. Because of this and the slightly higher f_{O_2} in the most

dust-enriched systems (800× and 1000×) a significant fraction of the Na condenses into the liquid above 1400 K. As a result, below 1400 K, Na_2O contents of the calculated liquids at dust enrichments of 800× and 1000× are in the range of those of many of the chondrules shown, and the calculated P_{Na} is very similar for all dust enrichments, varying from ~3.2 × 10^{-7} bar at a dust enrichment of 800× to ~4.8 × 10^{-7} bar at 1000× at
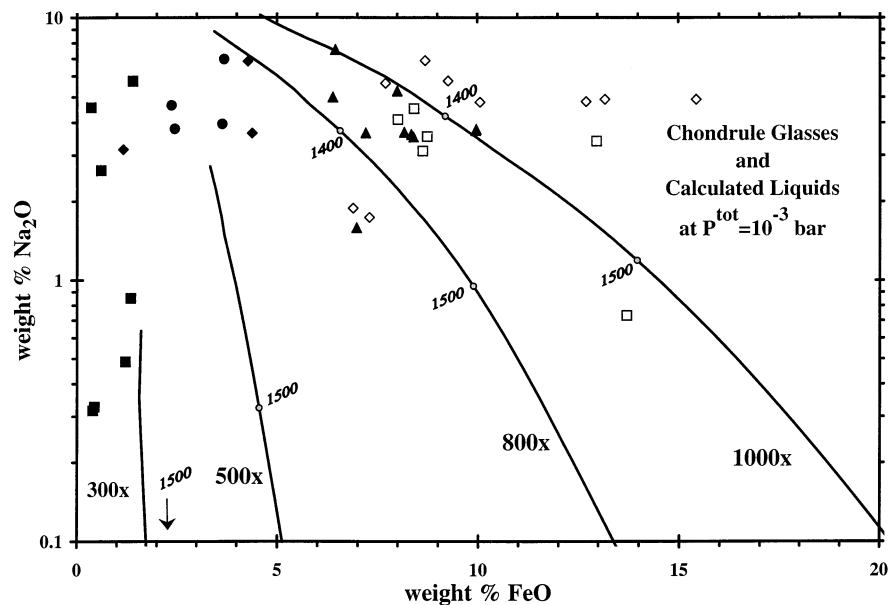

Fig. 19. Glass compositions in chondrules, with paths of condensate liquids for 300, 500, 800, and 1000× Cl dust enrichment, which terminate at their solidi. Data as in Fig. 18.

1350 K. The most important reason why the Na_2O contents of the liquids at the highest dust enrichments reach the levels found in chondrules, while those at the lowest dust enrichments (300× and 500×) do not is the persistence of the former to lower solidus temperatures, ~1300 K vs. ~1400 K (Fig. 8). As discussed above, this is due to higher FeO and Na_2O contents of the liquids in the more dust-enriched systems at 1400 K. At constant dust enrichment, our calculations show that maximum alkali contents of the liquids decrease substantially with decreasing P^{tot}. Even at P^{tot} as high as 10^{-4} bar and a dust enrichment of 1000×, for example, the maximum Na_2O content of the liquid is at least a factor of 5 smaller than at 10^{-3} bar and the same dust enrichment. Except for the type I chondrule glasses with Na_2O/FeO wt. ratios > 2.0, and type II chondrule glasses with very high FeO *and* Na_2O contents, all the chondrule glass compositions examined here could represent silicate liquids in equilibrium with dust-enriched vapor within 200° of their solidus temperatures at $P^{tot} > 10^{-4}$ bar. Even if the precursors of the most FeO- and Na_2O-rich chondrules were melted in a gas enriched 1000× by dust, their liquids would have lost sodium by evaporation or FeO by reduction, assuming that they were hot for a long enough time to have equilibrated with the gas.

5. CONCLUSIONS

Condensation of systems sufficiently enriched in dust of Cl composition to yield ferromagnesian silicates with molar FeO/(FeO + MgO) ratios of 0.1 to 0.4 at temperatures above 1200 K also produces copious molten silicate. The distribution of Fe between metal, silicate, and sulfide in specific classes of ordinary chondrites can be produced by high-temperature condensation at specific dust enrichments. While a rigorous thermodynamic model at last shows how direct condensation of silicate liquid can occur within the range of P^{tot} thought to have existed in the inner part of the solar nebula, the compositions of the partially molten condensates so formed do not match the compositions of types I and II chondrules in important ways. Such chondrules are thus secondary objects that did not form by direct condensation. Nevertheless, if chondritic matter owes its oxidation state to condensation of dust-enriched systems, the present work shows the sequence of condensation, details of the condensation reactions, and the evolution of the compositions of solid and liquid solution phases that may be relevant to the formation of chondrites and the precursors to chondrules. The present work also gives physico-chemical conditions capable of stabilizing against evaporation silicate liquids of specific compositions, some of which are similar to the compositions of some chondrule glasses, in cosmic gases at low nebular pressures.

REFERENCES

Anders E. and Grevesse N. (1989) Abundances of the elements: Meteoritic and solar. *Geochim. Cosmochim. Acta* **53,** 197–214.

Anderson G. M. and Crerar D. (1993) *Thermodynamics in Geochemistry*. Oxford U. Press.

Baker M. B., Hirschmann M. M., Ghiorso M. S., and Stolper E. M. (1995) Compositions of near-solidus peridotite melts from experiments and thermodynamic calculations. *Nature* **375,** 308–311.

Barin I. (1989) *Thermochemical data of pure substances*. VCH.

Berman R. G. (1983) A thermodynamic model for multicomponent melts, with application to the system CaO–MgO–Al_2O_3–SiO_2. Ph.D., Univ. British Columbia.

Berman R. G. (1988) Internally-consistent thermodynamic data for minerals in the system Na_2O–K_2O–CaO–MgO–FeO–Fe_2O_3–Al_2O_3–SiO_2–TiO_2–H_2O–CO_2. *J. Petrol.* **29,** 445–522.

Berman R. G. and Brown T. H. (1985) Heat capacity of minerals in the system Na_2O–K_2O–CaO–MgO–FeO–Fe_2O_3–Al_2O_3–SiO_2–TiO_2–H_2O–CO_2. *Contrib. Mineral. Petrol.* **89,** 168–183.

Betts J. T. (1980) A compact algorithm for computing the stationary point of a quadratic function subject to linear constraints. *ACM (Association for Computing Machinery) Trans. Mathematical Software* **6,** 391–397.

Charlu T. V., Newton R. C., and Kleppa O. J. (1981) Thermochemistry of synthetic $Ca_2Al_2SiO_7$ (gehlenite)–$Ca_2MgSi_2O_7$ (åkermanite) melilites. *Geochim. Cosmochim. Acta* **45,** 1609–1617.

Chase M. W., Jr., Davies C. A., Downey J. R., Frurip D. J., McDonald R. A., and Syverud A. N. (1985) *JANAF Thermochemical Tables*, 3rd ed. *J. Phys. Chem. Ref. Data* **14,** Suppl. 1.

Chuang Y.-Y., Hsieh K.-C., and Chang Y. A. (1986a) Thermodynamics and phase relationships of transition metal-sulfur systems: Part V. A reevaluation of the Fe–S system using an associated solution model for the liquid phase. *Metall. Trans.* **16B,** 277–285.

Chuang Y.-Y., Hsieh K.-C., and Chang Y. A. (1986b) A thermodynamic analysis of the phase equilibria of the Fe–Ni system above 1200 K. *Metall. Trans.* **17A,** 1373–1380.

Connolly H. C., Jr. and Burnett D. S. (1999) Minor element distributions in spinels from Type B CAI: An experimental study. *Lunar Planet. Sci.* **XXX,** Abstract #1459 (CD-ROM).

DeHart J. M., Sears D. W. G., and Lofgren G. E. (1988) Sodium enriched luminescent chondrule mesostasis rims in the unequilibrated ordinary chondrites. *Meteoritics* **23,** 265 (abstr.).

Dodd R. T. (1978) The composition and origin of large microporphyritic chondrules in the Manych (L-3) chondrite. *Earth Planet. Sci. Lett.* **39,** 52–66.

Ebel D. S. and Grossman L. (1996) Limiting conditions for silicate liquid stability in cosmic gases. *Meteoritics Planet. Sci. Suppl.* **31,** A40–A41 (abstr.).

Ebel D. S. and Grossman L. (1997a) Direct condensation of ferromagnesian liquids from cosmic gases. *Lunar Planet. Sci.* **XXVIII,** 317–318 (abstr.).

Ebel D. S. and Grossman L. (1997b) Stability of alkali and iron oxides in condensate liquids. *Meteoritics Planet. Sci. Suppl.* **32,** A37 (abstr.).

Ebel D. S. and Grossman L. (1998) Effect of dust enrichment on solid and liquid compositions in equilibrium with cosmic gases. *Lunar Planet. Sci.* **XXIX,** Abstract #1421 (CD-ROM).

Ebel D. S., Ghiorso M. S., Sack R. O., and Grossman L. (1999) Gibbs energy minimization in gas + liquid + solid systems. Submitted to *J. Computational Chem.*

Elkins L. T. and Grove T. L. (1990) Ternary feldspar experiments and thermodynamic models. *Am. Mineral.* **75,** 544–559.

Fegley B. J., Jr. (1981) The thermodynamic properties of silicon oxynitride. *J. Am. Ceram. Soc.* **64,** C-124–C-126.

Fegley B. J., Jr. and Palme H. (1985) Evidence for oxidizing conditions in the solar nebula from Mo and W depletions in refractory inclusions in carbonaceous chondrites. *Earth Planet. Sci. Lett.* **72,** 311–326.

Ghiorso M. S. (1985) Chemical mass transfer in magmatic processes I. Thermodynamic relations and numerical algorithms. *Contrib. Mineral. Petrol.* **90,** 107–120.

Ghiorso M. S. (1990) Thermodynamic properties of hematite–ilmenite–geikielite solid solutions. *Contrib. Mineral. Petrol.* **104,** 645–667.

Ghiorso M. S. (1994) Algorithms for the estimation of phase stability in heterogeneous thermodynamic systems. *Geochim. Cosmochim. Acta* **58,** 5489–5501.

Ghiorso M. S. and Carmichael I. S. E. (1985) Chemical mass transfer in magmatic processes II. Applications in equilibrium crystallization, fractionation and assimilation. *Contrib. Mineral. Petrol.* **90**, 121–141.

Ghiorso M. S. and Sack R. O. (1995) Chemical mass transfer in magmatic processes IV. A revised and internally consistent thermodynamic model for the interpolation and extrapolation of liquid–solid equilibria in magmatic systems at elevated temperatures and pressures. *Contrib. Mineral. Petrol.* **119**, 197–212.

Ghiorso M. S., Carmichael I. S. E., Rivers M. L., and Sack R. O. (1983) The Gibbs free energy of mixing of natural silicate liquids; an expanded regular solution approximation for the calculation of magmatic intensive variables. *Contrib. Mineral. Petrol.* **84**, 107–145.

Grønvold F. and Stølen S. (1992) Thermodynamics of iron sulfides II. Heat capacity and thermodynamic properties of FeS and of $Fe_{0.875}S$ at temperatures from 298.15 K to 1000 K, of $Fe_{0.98}S$ from 298.15 K to 800 K, and of $Fe_{0.89}S$ from 298.15 K to about 650 K. Thermodynamics of formation. *J. Chem. Thermodyn.* **24**, 913–936.

Grossman J. N., Alexander C. M. O'D., and Wang J. (1997) Zoning of trace elements and deuterium in the mesostasis of low-FeO chondrules in Semarkona. *Lunar Planet. Sci.* **XXVIII**, 481–482 (abstr.).

Grossman L. (1972) Condensation in the primitive solar nebula. *Geochim. Cosmochim. Acta* **36**, 597–619.

Hirschmann M. (1991) Thermodynamics of multicomponent olivines and the solution properties of (Ni, Mg, Fe)$_2$SiO$_4$ and (Ca, Mg, Fe)$_2$SiO$_4$ olivines. *Am. Mineral.* **76**, 1232–1248.

Hirschmann M. M., Ghiorso M. S., Wasylenki L. E., Asimow P. D., and Stolper E. M. (1998) Calculation of peridotite partial melting from thermodynamic models of minerals and melts I: Methods and comparison with experiments. *J. Petrol.* **39**, 1091–1115.

Hsieh K.-C., Chang Y. A., and Zhong T. (1982) The Fe–Ni–S system above 700°C (iron–nickel–sulfur). *Bull. Alloy Phase Diagrams* **3**, 165–172.

Hsieh K.-C., Vlach K. C., and Chang Y. A. (1987) The Fe–Ni–S system I. A thermodynamic analysis of the phase equilibria and calculation of the phase diagram from 1173 to 1623 K. *High Temp. Sci.* **23**, 17–37.

Ikeda Y. and Kimura M. (1985) Na–Ca zoning of chondrules in Allende and ALHA-77003 carbonaceous chondrites. *Meteoritics* **20**, 670–671 (abstr.).

Jarosewich E. (1990) Chemical analyses of meteorites: A compilation of stony and iron meteorite analyses. *Meteoritics* **25**, 323–337.

Jones R. H. (1990) Petrology and mineralogy of type II, FeO-rich chondrules in Semarkona LL3.0: Origin by closed-system fractional crystallization, with evidence for supercooling. *Geochim. Cosmochim. Acta* **54**, 1795–1802.

Jones R. H. (1994) Petrology of FeO-poor, porphyritic pyroxene chondrules in the Semarkona chondrite. *Geochim. Cosmochim. Acta* **58**, 5325–5340.

Jones R. H. (1996) FeO-rich, porphyritic pyroxene chondrules in unequilibrated chondrites. *Geochim. Cosmochim. Acta* **16**, 3115–3138.

Jones R. H. and Scott E. R. D. (1989) Petrology and thermal history of type IA chondrules in the Semarkona (LL3.0) chondrite. *Proc. 19th Lunar Planet. Sci. Conf.*, 523–536.

Knacke O., Kubaschewski O., and Hesselmann K. (1991) *Thermochemical Properties of Inorganic Substances.* Springer-Verlag.

Lattimer J. M., Schramm D. N., and Grossman L. (1978) Condensation in supernova ejecta and isotopic anomalies in meteorites. *Astrophys. J.* **219**, 230–249.

Lewis R. D., Lofgren G. E., Franzen H. F., and Windom K. E. (1993) The effect of Na vapors on the Na content of chondrules. *Meteoritics* **28**, 622–628.

Lofgren G. E. (1996) A dynamic crystallization model for chondrule melting. In *Chondrules and the Protoplanetary Disk* (eds. R. H. Hewins *et al.*), pp. 187–196. Cambridge U. Press.

Lux G., Keil K., and Taylor G. J. (1981) Chondrules in H3 chondrites: Textures, compositions and origins. *Geochim. Cosmochim. Acta* **45**, 675–685.

Normanton A. S., Moore R. H., and Argent B. B. (1976) A calorimetric and mass-spectrometric study of solid iron–chromium alloys. *Metal Sci.* **10**, 207–213.

Palme H. and Fegley B. J., Jr. (1990) High-temperature condensation of iron-rich olivine in the solar nebula. *Earth Planet. Sci. Lett.* **101**, 180–195.

Pedley J. B. and Marshall E. M. (1983) Thermochemical data for gaseous monoxides. *J. Phys. Chem. Ref. Data* **12**, 967–981.

Petaev M. I. and Wood J. A. (1998) Mineral equilibrium in fractionated nebular systems. II. A new code embracing 18 elements. *Lunar Planet. Sci.* **XXIX**, Abstract #1474 (CD-ROM).

Radomsky P. M. and Hewins R. H. (1990) Formation conditions of pyroxene–olivine and magnesian olivine chondrules. *Geochim. Cosmochim. Acta* **54**, 3475–3490.

Robie R. A., Hemingway B. S., and Fisher J. R. (1978) Thermodynamic properties of minerals and related substances at 298.15 K and 1 bar (10^5 Pascals) pressure and at higher temperatures. USGS Bull. 1452.

Rubin A. and Wasson J. T. (1986) Chondrules in the Murray CM2 meteorite and compositional differences between CM–CO and ordinary chondrite chondrules. *Geochim. Cosmochim. Acta* **50**, 307–315.

Rubin A., Fegley B. J., Jr., and Brett R. (1988) Oxidation state in chondrites. In *Meteorites and the Early Solar System* (eds. J. F. Kerridge and M. S. Matthews), pp. 488–511. U. Arizona Press.

Sack R. O. and Ghiorso M. S. (1989) Importance of considerations of mixing properties in establishing an internally consistent thermodynamic database: Thermochemistry of minerals in the system Mg$_2$SiO$_4$–Fe$_2$SiO$_4$–SiO$_2$. *Contrib. Mineral. Petrol.* **102**, 41–68.

Sack R. O. and Ghiorso M. S. (1991a) An internally consistent model for the thermodynamic properties of Fe–Mg–titanomagnetite–aluminate spinels. *Contrib. Mineral. Petrol.* **106**, 474–505.

Sack R. O. and Ghiorso M. S. (1991b) Chromian spinels as petrogenetic indicators: Thermodynamic and petrological applications. *Am. Mineral.* **76**, 827–847.

Sack R. O. and Ghiorso M. S. (1994a) Thermodynamics of multicomponent pyroxenes: I. Formulation of a general model. *Contrib. Mineral. Petrol.* **116**, 277–286.

Sack R. O. and Ghiorso M. S. (1994b) Thermodynamics of multicomponent pyroxenes: II. Phase relations in the quadrilateral. *Contrib. Mineral. Petrol.* **116**, 287–300.

Sack R. O. and Ghiorso M. S. (1994c) Thermodynamics of multicomponent pyroxenes: III. Calibration of $Fe^{2+}(Mg)_{-1}$, $TiAl_2(MgSi_2)_{-1}$, $TiFe^{3+}_2(MgSi_2)_{-1}$, $AlFe^{3+}(MgSi)_{-1}$, $NaAl(CaMg)_{-1}$, $Al_2(MgSi)_{-1}$ and $Ca(Mg)_{-1}$ exchange reactions between pyroxenes and silicate melts. *Contrib. Mineral. Petrol.* **118**, 271–296.

Sakao H. and Elliott J. F. (1975) Thermodynamics of dilute bcc Fe–Si alloys. *Metal. Trans.* **6A**, 1849–1851.

Sharp C. M. and Wasserburg G. J. (1995) Molecular equilibria and condensation temperatures in carbon-rich gases. *Geochim. Cosmochim. Acta* **59**, 1633–1652.

Simon S. B. and Haggerty S. E. (1979) Petrography and olivine mineral chemistry of chondrules and inclusions in the Allende meteorite. *Proc. 10th Lunar Planet. Sci. Conf.*, 871–883.

Smith W. R. and Missen R. W. (1982) *Chemical Reaction Equilibrium Analysis: Theory and Algorithms.* Wiley.

Sorby H. C. (1877) On the structure and origin of meteorites. *Nature* **15**, 495–498.

Steele I. M. (1986) Compositions and textures of relic forsterite in carbonaceous and unequilibrated ordinary chondrites. *Geochim. Cosmochim. Acta* **50**, 1379–1395.

Stull D. R. and Prophet H. (1970) *JANAF Thermochemical Tables*, 2nd ed. U.S. National Bureau of Standards.

Takahashi E. (1986) Melting of a dry peridotite KLB-1 up to 14 GPa: Implications on the origin of peridotitic upper mantle. *J. Geophys. Res.* **91**, 9367–9382.

Takahashi E., Shimazaki T., Tsuzaki Y., and Yoshida H. (1993) Melting study of a peridotite KLB-1 to 6.5 GPa, and the origin of basaltic magmas. *Philos. Trans. R. Soc. London A* **342**, 105–120.

Tsuchiyama A., Nagahara H., and Kushiro I. (1981) Volatilization of sodium from silicate melt spheres and its application to the formation of chondrules. *Geochim. Cosmochim. Acta* **45**, 1357–1367.

Van Schmus W. R. (1969) The mineralogy and petrology of chondritic meteorites. *Earth-Science Rev.* **5**, 145–184.

Wagner R. D. (1979) The condensation and stability of chemically heterogeneous systems, M.S. thesis. Arizona State University.

Wark D. A. (1987) Plagioclase-rich inclusions in carbonaceous chon-

drite meteorites: Liquid condensates? *Geochim. Cosmochim. Acta* **51,** 221–242.

Weinbruch S., Palme H., Müller W. F., and El Goresy A. (1990) FeO-rich rims and veins in Allende forsterite: Evidence for high temperature condensation at oxidizing conditions. *Meteoritics* **25,** 115–125.

Whipple F. L. (1966) Chondrules: Suggestion concerning the origin. *Science* **153,** 54–56.

Wood J. A. (1967) Olivine and pyroxene compositions in type II carbonaceous chondrites. *Geochim. Cosmochim. Acta* **31,** 2095–2108.

Wood J. A. (1984) On the formation of meteoritic chondrules by aerodynamic drag heating in the solar nebula. *Earth Planet. Sci. Lett.* **70,** 11–26.

Wood J. A. and Hashimoto A. (1993) Mineral equilibrium in fractionated nebular systems. *Geochim. Cosmochim. Acta* **57,** 2377–2388.

Wood J. A. and Morfill G. E. (1988) Solar nebula models. In *Meteorites and the Early Solar System* (eds. J. F. Kerridge and M. S. Matthews), pp. 329–347. Univ. Arizona Press.

Yoneda S. and Grossman L. (1995) Condensation of CaO–MgO–Al$_2$O$_3$–SiO$_2$ liquids from cosmic gases. *Geochim. Cosmochim. Acta* **59,** 3413–3444.

Yu Y. and Hewins R. (1998) Transient heating and chondrule formation: Evidence from sodium loss in flash heating simulation experiments. *Geochim. Cosmochim. Acta* **62,** 159–172.